34

Related Methods for Three-Dimensional Imaging

J. Michael Tyszka, Seth W. Ruffins, Jamey P. Weichert, Michael J. Paulus, and Scott E. Fraser

INTRODUCTION

The ability of confocal laser-scanning microscopy to collect stacks of optical sections has made three-dimensional (volumetric) imaging a standard analytical tool in experimental cell and developmental biology. Parallel developments in deconvolution techniques, especially as computational power increased and costs decreased, offered tools to make three-dimensional (3D) imaging from widefield as well as confocal microscopes possible. Despite the high spatial resolution provided by these 3D methods, they all suffer from a common limitation: light scattering in the specimen limits them to operating in the outer few hundred micrometers of the specimen. Even the greater depth of penetration and reduced photobleaching provided by two-photon laser-scanning microscopy falls short for larger specimens such as embryos. To perform volumetric imaging on larger specimens, alternative approaches are needed. This chapter examines four light-optical methods: surface imaging microscopy (SIM), optical coherence tomography (OCT), optical projection tomography (OPT), and the recently developed selective plane illumination microscope (SPIM), as well as microscopic magnetic resonance imaging (µMRI) and microscopic computed tomography (CT) as potential solutions to the challenges of collecting high-quality 3D image data.

Each of these volumetric imaging methodologies has particular strengths and limitations; no single method addresses all 3D imaging requirements. SIM (also referred to as episcopic fluorescence image capture (EFIC) takes a brute force approach, physically sectioning the specimen and obtaining a series of two-dimensional images that can later be assembled into a volumetric reconstruction. Both OPT and OCT employ different tomographic approaches to obtain data from the depth of the specimen, building up a 3D model from a series of 2D data sets. OPT transilluminates the specimen, and collects a large number of 2D images from different orientations; OCT uses depth encoding of reflected light and is conceptually similar to ultrasound imaging. SPIM represents a hybrid between these approaches, using transverse, sheet-like illumination to generate series of 2D image stacks from different orientations that can be assembled with computational tools. Finally, µMRI and micro-computerized tomography (micro-CT) are non-optical. The former derives image contrast from the water contained in the specimen. This permits the entire volume of an opaque object to be imaged. The latter is merely a micro version of the CAT scanner used in hospitals. We will describe each of these techniques and suggest how each might be used.

SURFACE IMAGING MICROSCOPY AND EPISCOPIC FLUORESCENCE IMAGE CAPTURE

Surface imaging microscopy is a form of physical serial sectioning where one images the cut face of the embedded specimen instead of the ribbon of removed sections.

A SIM/EFIC device is essentially a widefield microscope mounted on a precision microtome. Dry objectives ranging from 2× to 40× magnification are used to image the face of the embedding block to an in-plane resolution of 8.8 to 0.4 µm, respectively. As each section is cut, the face of the remaining block is recorded with a charge-coupled device (CCD) camera (Ewald *et al*., 2002, 2004; Weninger and Mohun, 2002) (Fig. 34.1). The stack of images is then reconstructed into a high-resolution image volume.

Imaging the block face rather than the ribbon has significant advantages. The mass of embedding medium supports the specimen and minimizes sectioning artifacts such as compression, folding, and tearing. Perfectly-registered data volumes are easily reconstructed as the block face is photographed at the same position in the microtome's sectioning cycle.

SIM/EFIC is a fluorescence imaging modality that relies on endogenous autofluorescence or exogenous dye labeling of the specimen. To prevent out-of-focus fluorescence from compromising image quality, specimens are embedded in highly light absorbent black paraffin or dark embedding resins; the opacity of the embedding medium can be adjusted to match the in-plane resolution of the objective being used and the section thickness, producing isotropic image volumes (Fig. 34.2). SIM can produce stunning 3D image volumes with isotropic voxel resolutions of ~0.5 µm.

At such high resolution, individual cell morphology can be examined within the context of tissues and entire organisms. SIM has been used in morphogentic studies to reveal the relationship between cell morphology and overall tissue shape and to follow the changes that occur during embryonic development (Ewald *et al*., 2002). SIM has also been used in the materials sciences to understand how microscopic structure relates to the strength, feel, texture, and other properties of textiles and papers.

SIM, however, is a destructive imaging modality that allows no other data collection from a given specimen. In combination with the non-destructive methods discussed below, SIM can be used to add a content-rich description of a single specimen.

J. Michael Tyszka, Seth W. Ruffins, and Scott E. Fraser • California Institute of Technology, Pasadena, California 91125
Jamey P. Weichert • University of Wisconsin, Madison, Wisconsin 53706
Michael J. Paulus • ORNL and CTI-Concorde Microsystems, Knoxville, Tennessee 37932

Handbook of Biological Confocal Microscopy, Third Edition, edited by James B. Pawley, Springer Science+Business Media, LLC, New York, 2006.

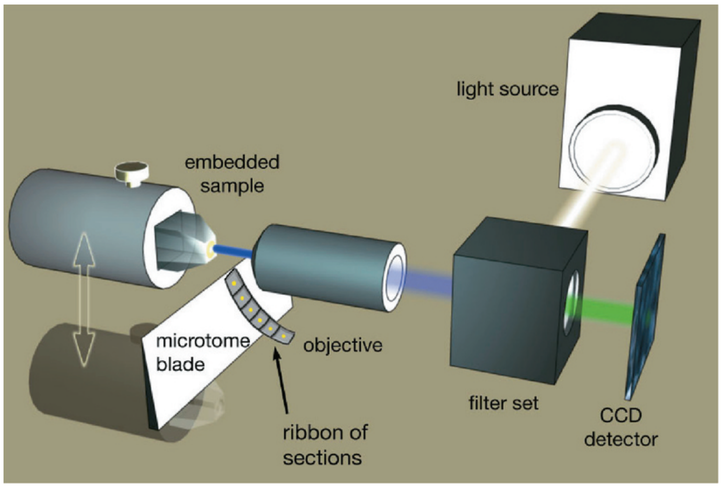

FIGURE 34.1. Surface imaging microscopy/episcopic fluorescence image capture setup. SIM/EFIC is a block-face imaging modality. Essentially, a microtome is outfitted with a microscope imaging system. A sample is embedded in an opaque medium and sectioned using a diamond knife. A horizontally-mounted microscope captures an image of the block face as the chuck returns to a specific position after each section is cut. The resulting image series is reconstructed into a perfectly-registered image volume with high resolution.

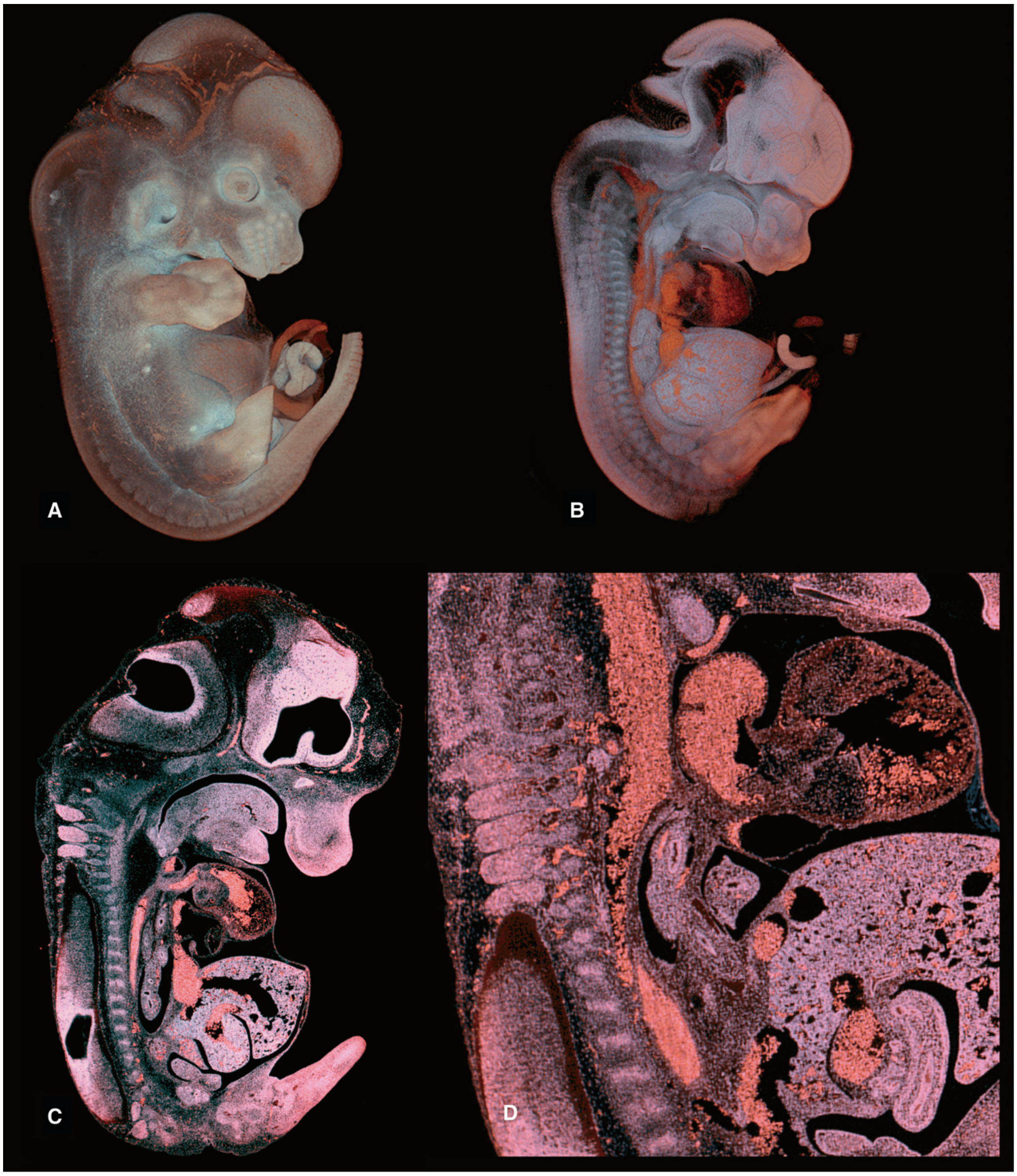

FIGURE 34.2. SIM of 12.5 dpc mouse embryo stained with fluorescent analog of H&E staining. The image volume was collected with a 2× objective and provides approximately 8 µm/pixel resolution. This data volume is 1517 × 1016 × 664 pixels. (A) Whole embryo view shows external structures with high fidelity. (B) A slab section ~1700 µm thick. (C) A single section through the embryo, and (D) the high magnification view. SIM provides a global view of the specimen at near cellular resolution.

OPTICAL COHERENCE TOMOGRAPHY

Optical coherence tomography (Huang *et al*., 1991; Tearney *et al*., 1997; Masters, 1999) is well suited to examining tissue geometry and organization, even in living, unstained tissues (Boppart *et al*., 1996, 1997, 1998; Yazdanfar *et al*., 1997; Rollins *et al*., 1998). OCT is based upon the reflection/backscattering of light and is not unlike sonar, detecting the amount of light reflected from different depths (up to a few millimeters) in the specimen to build up a voxel-by-voxel image. The challenge of OCT is to optically section the huge amount of backscattered light to create an image of a single plane at depths several-fold greater than the mean free path of light in the specimen. To meet this challenge, OCT uses interference between the light reflected by the specimen and the light reflected by a reference mirror to isolate individual optical sections.

Although its ability to image deep in a specimen far outperforms confocal microscopy, an OCT shares many features with the optics of a reflected light confocal microscope. An OCT microscope images the output of an optical fiber through an objective lens, and re-images the backscattered signal from specimen into the same fiber, creating a confocal aperture; the difference is that an OCT uses a short coherence length light source and an interferometer to add a "coherence gate" that suppresses the signal from out-of-focus planes by 6 orders of magnitude (Rollins and Izatt, 1999). The Michelson interferometer of a typical OCT is created from optical fibers; the beam-splitter is created by fusing the two optical fibers into a 2 × 2 coupler. The reference arm fiber is terminated with a collimating lens and retro-reflector; the specimen arm is terminated by a collimating lens, beam-steering galvonometers, and an imaging lens such as a microscope objective. Both the length of the two arms and the materials must be closely matched to avoid unequal group velocity dispersion in the specimen and reference arms. The creation of interference fringes involves modulating the length of the arms by means ranging from stretching the optical fibers with piezoelectric devices to a grating-based phase-delay retro-reflector.

In an OCT, the signal is derived from interference fringes, as light back-reflected from the reference mirror and the specimen interferes coherently. Fringes will only result if the optical path lengths of the reference and specimen arms are equal to within half of the coherence length of the light source (the "coherence gate"). Signal from multiply-scattered photons are rejected by the concerted action of the confocal aperture and the coherence gate. The frequency of the interference fringes is set by the motion of the reference reflector (or interferometer arms), giving the detection electronics a defined lock-in frequency to detect, and thereby rejecting the signal from light that is backscattered (but not interfering) from above and below the focal plane. Thus, resolution of an OCT microscope is set by two factors: the coherence length of the light source (for depth) and the size of the illuminated spot (for lateral resolution).

A typical OCT generates a scan perpendicular to the surface, much like the *xz*-scans generated in confocal microscopy, creating a slice through the depth of the specimen (Fig. 34.3). A galvonometer mirror translates the beam in one axis; at each spot along this line, a rapid change in the length of the reference arm (changing the length or the retro-reflector position) scans the coherence volume by millimeters. Such a rapid depth scan with a slower lateral scan creates an image reminiscent of that created by ultrasonography. Volumetric (3D) images can be assembled by collecting a series of neighboring depth scans. OCT scans can be generated quickly, with depth discrimination set by the coherence length of the light source; however, the lateral resolution of the images is typically compromised because the coherence volume must move very rapidly in depth, much more rapidly than it is possible to refocus the light in the specimen. As a result, the lens focusing the light into the specimen must employ a relatively shallow convergence angle so that the spot size does not change too dramatically over the ±2 mm motion of the coherence volume in depth. Thus, B-mode instruments often achieve resolutions of less than 10 µm in depth, but greater than 10 µm in lateral extent (see Izatt *et al*., 1996). Given the laminar organization of many

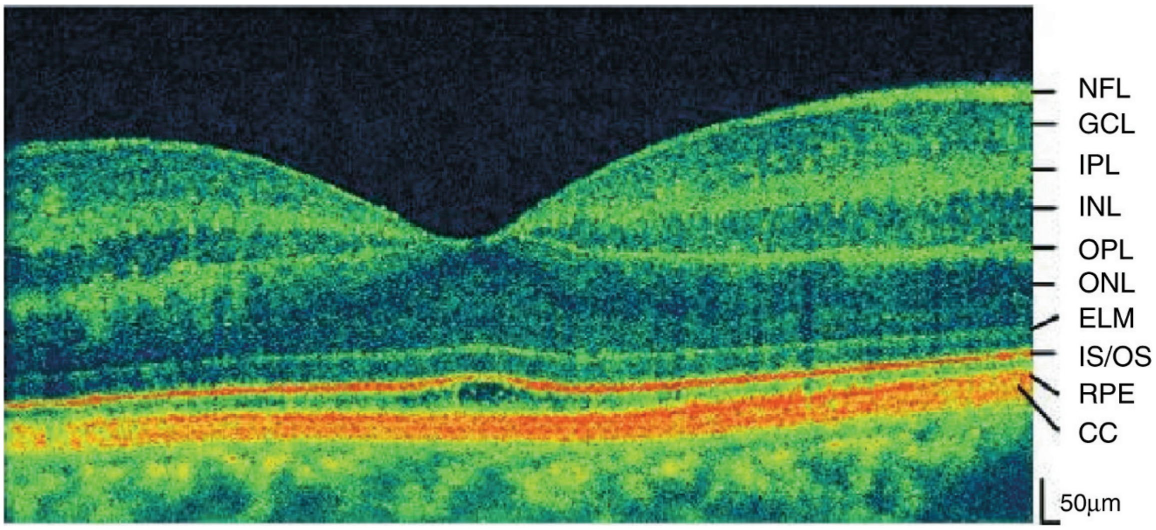

FIGURE 34.3. *In vivo* ultrahigh resolution OCT B mode (*xz*) section through a human retina, viewed through the cornea. A depth resolution of less than 5 microns was achieved using a very broad bandwidth light source. Transverse resolution was limited by the numerical aperture of the lens in the human eye and by imperfections in its optical characteristics. Abbreviations: NFL = Nerve Fiber Layer, GCL = Ganglion Cell Layer, IPL = Inner Plexiform Layer, INL = Inner Nuclear Layer, OPL = Outer Plexiform Layer, ONL = Outer Nuclear Layer, ELM = External Limiting Membrane, IS/OS = Photoreceptor Inner/Outer Segment Junction, RPE = Retinal Pigment Epithelium, CC = *Choriocapillaris*. (Reproduced with permission from Wojtkowski, 2004 © Optical Society of America.)

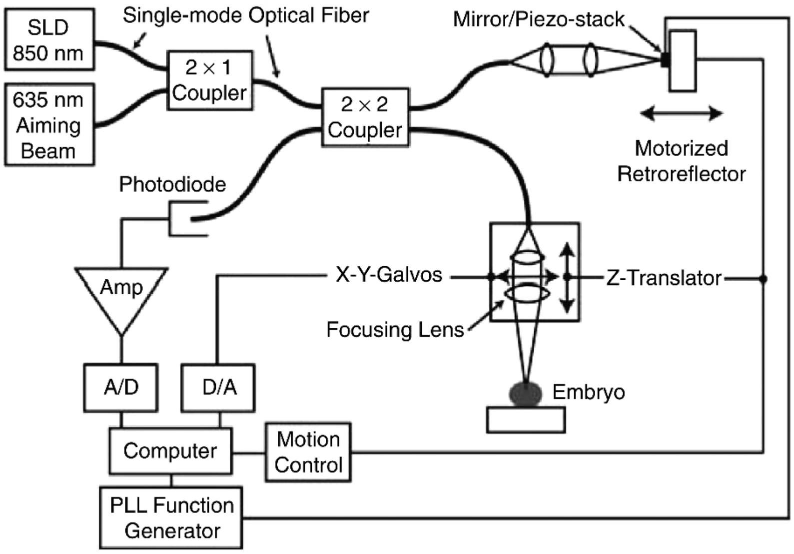

FIGURE 34.4. Schematic of an *en face* OCT system. The superluminescent diode (SLD), which provides the broad bandwidth light for OCT imaging, is combined with an alignment laser diode at 635 nm using a 2 × 1 coupler. The 2 × 2 coupler splits the light between the sample arm with the focusing lens and the reference arm with the motorized retro-reflector. The reflected light from both arms interferes and is measured by the photodiode at the output of the 2 × 2 coupler. Electronic demodulation of the photodiode signal produces an OCT signal for a given depth position in the sample. Transverse scanning and subsequent depth scanning produce a 2D *en face* image and a 3D image, respectively. (Reproduced with permission from Haskell *et al.*, 2004 © IEEE.)

specimens, such as the layered organization of the retina, striking images can result.

En face OCT is an alternative approach for OCT imaging that can optimize lateral resolution by using a higher numerical-aperture (NA) imaging lens (Hoeling *et al.*, 2000, 2001). A smaller spot size, more similar to that used in confocal microscopy is created, and galvomometer mirrors are used to scan the beam through a complete optical section (Fig. 34.4). The focal depth and coherence depth must be aligned to the same optical section by the positioning of the retro-reflector. Interference fringes are generated by changing the length of the reference arm, typically by oscillating a small mirror or by using an acousto-optical device, by an amount far less than the coherence length. Thus, the depth resolution is set at roughly half the coherence length of the light source. Volumetric images are built up from collecting a series of 2D (*en face*) scans, adjusting the focus (and coherence depth) after each scan to build up a *z*-series of images (Fig. 34.5). Given the performance of inexpensive wide-bandwidth light sources, and the index of refraction of tissue (>1.3), *en face* OCT microscopy can generate images with isotropic resolution of ~5 µm.

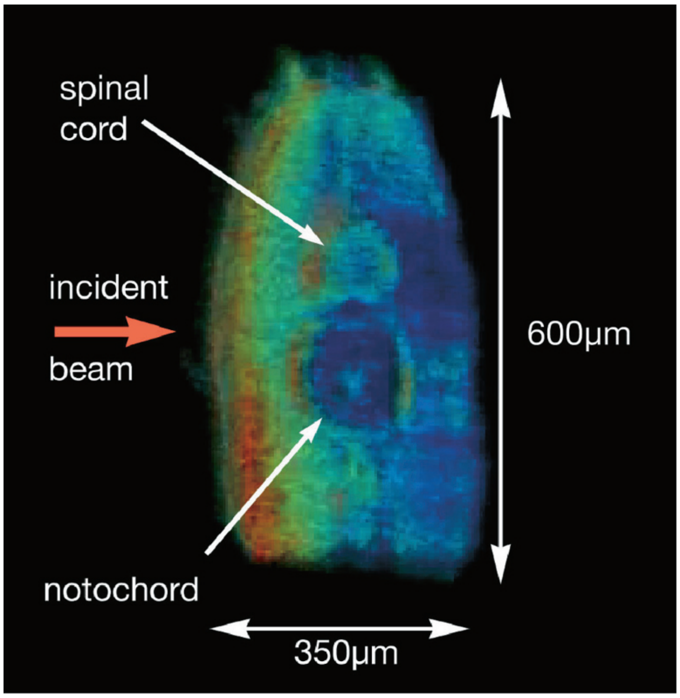

FIGURE 34.5. OCT section of a paraformaldehyde-fixed stage 41 *Xenopus laevis* embryo viewed along the spinal cord from the tail towards the head with dorsal at the top of the figure. The beam is incident from the left side of the embryo and the colorscale encodes backscatter intensity from blue (low) to red (high). (Reproduced with permission from Hoeling *et al.*, 2000. © Optical Society of America.)

OPTICAL PROJECTION TOMOGRAPHY

Optical projection tomography is a projection tomographic method akin to X-ray computed axial tomography (commonly called CT or CAT, see micro-CT below) and electron microscopy tomography (EMT). Like other projection tomogram methods, OPT uses 2D projections of 3D objects to reconstruct the volume of an object using a Radon-backplane reconstruction algorithm (for review, see Herman, 1980). Each point in the projected image is the result of the cumulative absorption or emission of light rays propagating through an object. OPT operates in both bright-field (transmission) and fluorescence (emission) modes and is proving useful in capturing patterns of gene expression and antibody staining *in situ*. Image volumes reconstructed from projection tomogram data differs from the optical and physical sectioning methods described above in that the location of features within an object are not explicitly sampled. Instead, the location of features is computed from a series of 2D projections collected from many axial positions around the object.

An OPT instrument is a relatively simple device consisting of a sample chamber with a rotating sample platform, imaging optics for capturing projections, and a diffuse light source for bright-field mode (Fig. 34.6). In fluorescence mode, the imaging optics are used for widefield illumination of the specimen. OPT requires that the specimen be transparent and indexed-matched with the surrounding media to permit light to pass through the object with minimal refraction. Currently this is achieved by clearing and imaging specimens in a mixture of benzyl alcohol and benzyl benzoate (BABB). Typically, a sample is suspended in agarose and

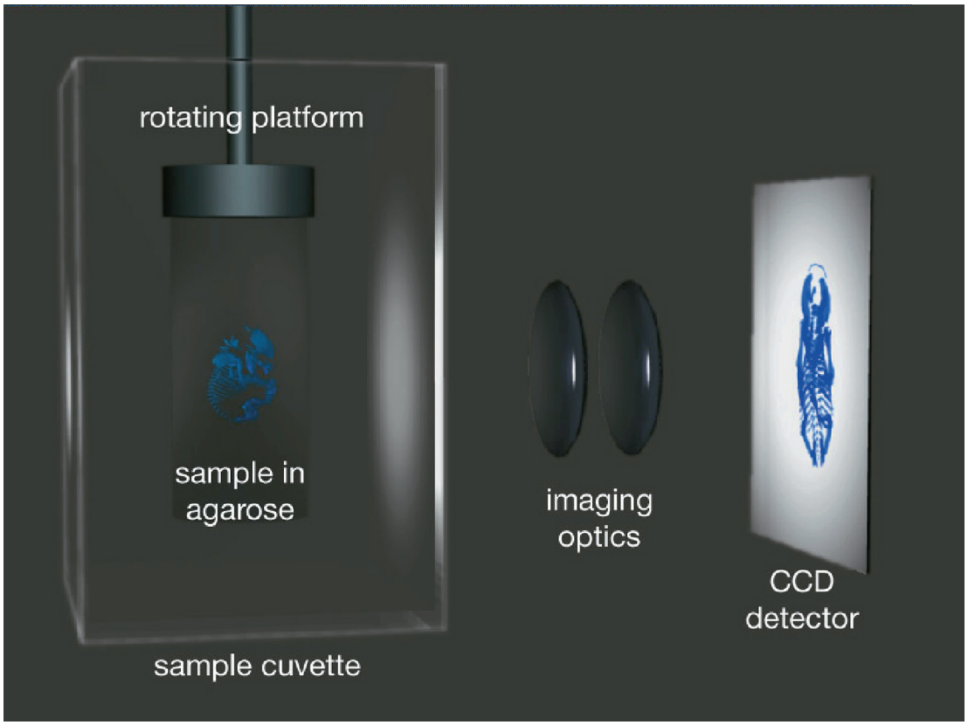

FIGURE 34.6. Optical projection tomography setup (bright-field mode). (A) Cleared specimen is suspended in agarose gel, mounted to a rotating platform, and placed in chamber containing indexed-matched media. Imaging optics (B) are used to focus the projected image and reject light scattered by the specimen. The projected image (C) is collected with a CCD camera. Multiple projections are used to reconstruct an image volume.

serially dehydrated in methanol and then cleared in BABB. The sample in the agarose block is placed onto the rotating stage in a sample chamber containing BABB (Sharpe *et al.*, 2002).

X-ray computed axial tomography (CAT or CT) and electron microscopy tomography (EMT) assume that the specimen is transparent to the probing rays and that refraction is non-existent. The paths of the projected rays are straight and produce a perfect "shadow projection." Because, in fact, the probing light rays are susceptible to scatter and some degree of diffraction and refraction as they pass through the specimen, the resulting projection is "confused" and blurred as it is composed of rays that have followed the predicted path through the subject as well as stray rays. The imaging optics focus the projection and collimate the rays that are projected along an approximately straight path through the sample (Fig. 34.7).

The limited depth of focus inherent in all optical microscope systems requires that modifications be made to the collection and projection reconstruction (Sharpe, 2004). Projections captured by OPT represent only the volume residing within the region of the depth of focus. During imaging, the center of focus is set to a plane approximately half the distance between the axis of rotation and the near side of the specimen. Because each projection only represents about half the specimen volume, a complete projection set requires the specimen be rotated through 360° at 0.9° intervals. Volume reconstruction is performed using a modified back-plane projection algorithm to compensate for the limited projected volume.

For small objects (on the order of 5 mm diameter) light scatter is not severe and internal details can be readily resolved. The

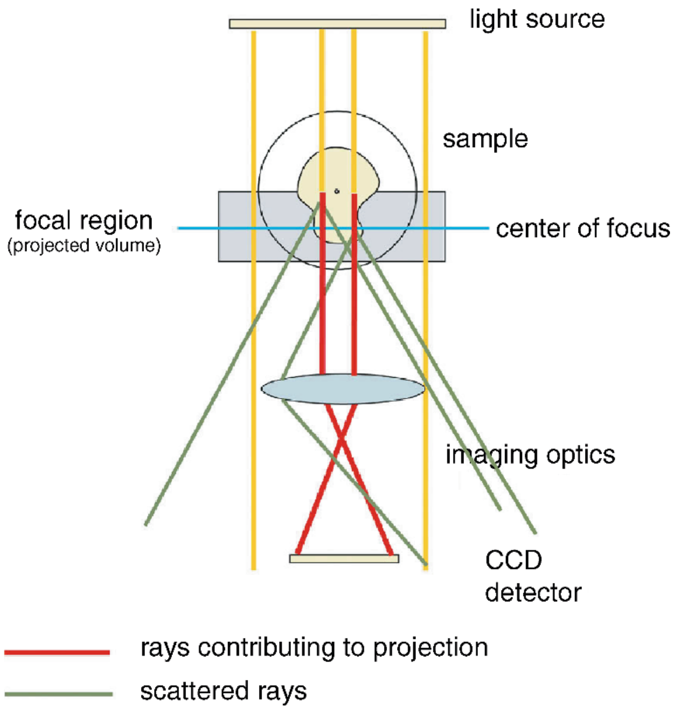

FIGURE 34.7. Due to the limited focal depth of the imaging optics, the focus is set to the region between the axis of rotation and the imaging optics. Each projection represents only half the specimen volume requiring that the subject be rotated through 360° to collect a full projection set.

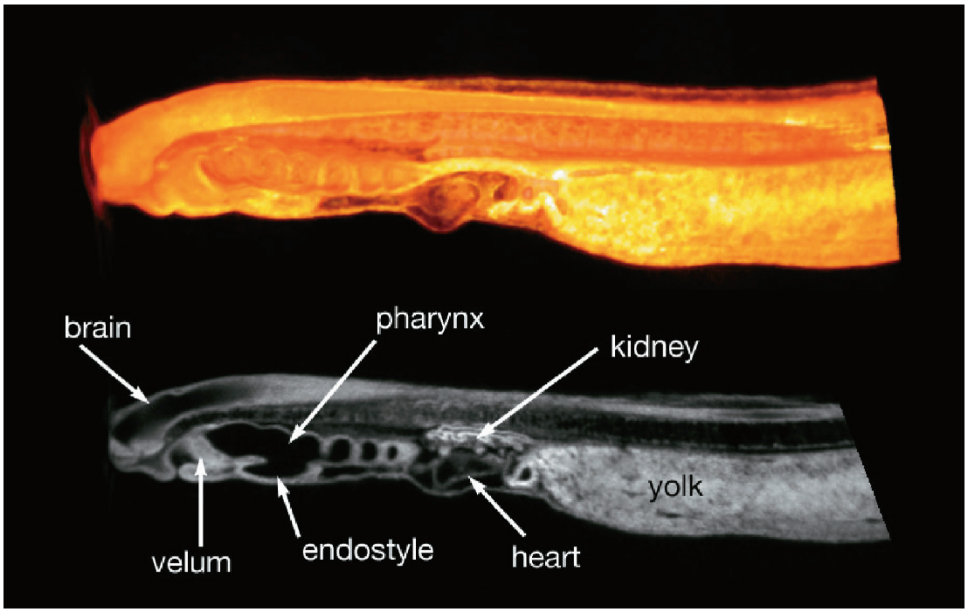

FIGURE 34.8. Autofluorescent OPT reconstruction of 17-day lamprey larva. The larva was imaged using a Texas Red filter set and mounted with the anterior–posterior axis (long axis) along the axis of rotation. The light path is between 1.5 to 3 mm (left–right, dorsal–ventral axis, respectively). The larva is virtually opaque in visible light yet internal structures are easily identifiable using near IR autofluorescence.

quality of the projections diminishes as the objects imaged become larger because of the increased light scattering. The result is that fewer internal details are resolved, and opaque regions, such as highly pigmented tissues, similarly degrade the projections (Fig. 34.5).

The time required to collect a complete projection set (400 images) ranges between 3 (for bright-field and strong fluorescent signals) and 15 min, depending on signal strength. Current reconstruction performance is about 6 min for a 512^3 voxel image volume on a standard 4 GHz Pentium 4 class workstation.

OPT has only recently become a practical device for routine 3D imaging, but it is proving to be useful as an analytical tool for developmental biology as it is capable of imaging anatomy, gene expression patterns and the distribution of specific cell populations, extracellular matrix components, etc., as revealed by antibody labeling. One of its first uses was to collect anatomical data of early human and mouse development for the creation of volumetric atlases for the analysis of aberrant embryogenesis (Sharpe, 2003; Kerwin *et al*., 2004; Robson *et al*., 2004).

The anatomy of unlabeled embryos can be collected in either bright-field and/or fluorescent modes. Each modality reveals different features depending on the wavelength of the probing light. In the bright-field mode, tissue transparency increases as the illumination moves into the near-infrared (IR), allowing deeper imaging of larger embryos. Structures that are opaque in visible light, such as the pigmented retina, can be imaged using transmitted light at these longer wavelengths. In the fluorescence mode, the vasculature is revealed as blood fluoresces brightly when Texas Red filter sets are used (562 nm excitation to 624 nm emission). The autofluorescence of the lamprey larva has been used to reveal internal structures without physical sectioning (Fig. 34.8). However, the information content within an embryo is not limited to its intrinsic optical properties. Cell- and tissue-specific chemical composition can be made visible using labeled antibodies and classic histological stains while RNA hybridization and green fluorescent protein (GFP) reporter constructs show gene activity. Many of these protocols are compatible with OPT imaging.

Bright-field OPT has successfully been used to image the intricate spatial arrangement of the developing skeleton using the common histological stain Alcian Blue (Fig. 34.9). *In situ* RNA

FIGURE 34.9. Bright-field OPT reconstruction of Alcian Blue stained 12.5 dpc mouse embryo. Non-ossified skeletal elements stained with Alcian Blue reveal the intricate and delicate structure of the fetal mouse. Note that dermal bone has not yet formed.

hybridization reveals the global pattern of specific gene activity using a color precipitate indicator. Standard whole-mount photography reveals regions of gene activity but sections are needed to define the precise location of expressing tissues and cells. Once sectioned, the 3D context is lost. Additionally, weak signals may not be detected in thin sections. OPT is a powerful tool in that a single imaging experiment places local and specific activity in the context of the entire embryo. Potentially, OPT may be able to capture weak signals as projections that are cumulative through the sample volume (up to 2 mm compared with 10–15 µm for histological sections).

OPT requires that the light rays be able to pass through the object with minimal scatter. This limits OPT use to transparent specimens with a homogeneous refractive index (RI). Thus far, OPT has primarily been used for fixed specimens but there is a potential for imaging live specimens, such as tissue explants and early embryogenesis of aquatic organisms. This method could be used for time-lapse studies with the shortest interval being the time required to acquire a full set of projections. Currently, the minimum time interval for collecting 400 projections is about 3 min but as there is a trade-off between spatial resolution and number of projections, one can acquire a smaller set of images more rapidly if one is willing to settle for less resolution.

LIGHT SHEET MICROSCOPY

"Light sheet" fluorescence microscopy, originally developed by Voie (1995, 2002), is an optical-sectioning technique whereby only the plane being imaged is illuminated. The concept is not unlike that of multi-photon microscopy in that only the fluorophores in the focus plane are excited, thus minimizing photodamage. Rather than using the imaging optics to illuminate the specimen, as in epi-fluorescence microscopes, light-sheet microscopy uses separate illumination optics to produce an illuminated layer perpendicular to the imaging axis. Optical sectioning is achieved by moving the light sheet through the specimen coincident with the focus plane of the imaging optics (also see Chapter 37, *this volume*).

Optical Setup

Selective plane illumination microscopy (SPIM) is the name given to an updated version of light-sheet microscopy developed by the Stelzer group at the EMBL/Heidelberg. In this system, the microscope optics are arranged horizontally to accommodate a cylindrical sample immersed in a fluid-filled sample chamber and capable of being rotated around its vertical axis. This arrangement provides an ideal environment for imaging living specimens as it permits the media to be replaced and additional agents, such as nutrients, growth factors, gases, etc., to be introduced during imaging. Samples are typically suspended in soft agarose and placed into the sample chamber containing liquid medium. The sample is imaged using a water dipping lens inserted through one wall of the sample chamber. Windows on the lateral walls (perpendicular to the imaging axis) allow the light sheet to illuminate the specimen. The light sheet is formed by passing collimated laser light through a cylindrical lens and controls are provided to adjust the thickness and convergence of this sheet (Huisken *et al.*, 2004) (Fig. 34.10).

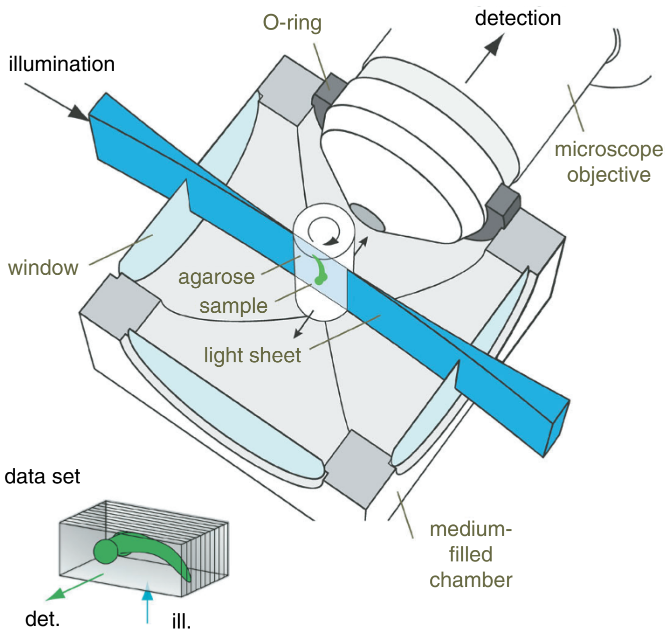

FIGURE 34.10. Selective plane illumination microscope (SPIM) setup. The specimen is suspended in agarose in a medium-filled sample chamber. The SPIM device optically sections the sample as it is illuminated by a "light sheet" perpendicular to the imaging axis and coincident with the focus plane of the imaging optics. The sample can be rotated to collect multiple views for the reconstruction of subjects that cannot be imaged through their entire volume.

The lateral (*xy*) resolution of SPIM is limited by the light scattering and absorption properties of the specimen being imaged while the axial (*z*) resolution is dependent on the thickness of the light sheet. The lateral penetration and scatter of the light sheet will affect the thickness and intensity of the illuminated layer across the field of view.

SPIM is an excellent imaging modality for transparent specimens such as Medaka and zebrafish embryos. Developing larval Medaka fish have been imaged to a depth of 500 µm with an axial resolution of 6 µm. The imaging depth, however, is not great enough to encompass the entire embryo and images of deeper structures are of a lower quality than those of features near the surface. A solution to this problem has been to collect multiple image stacks from different views of the specimen. Each view produces a set of data that includes information not available in other views. Combining the multiple views into a single image volume produces a reconstruction of the entire specimen. Entire volumes nearly 2 mm thick can be reconstructed at a voxel size of ~5 µm.

SPIM is also useful as a tool for capturing dynamic events on time scales ranging from fractions of a second to days. The use of a narrow light sheet plane allows widefield optics to be used, maximizing the emitted light collection without compromising axial resolution. Maximizing light collection minimizes the excitation time required for each image. Short exposure times minimize photodamage and permit long-term imaging experiments. The use of high-speed cameras allows SPIM to be used for observing dynamic events such as the beating heart of a Medaka embryo (Fig. 34.11).

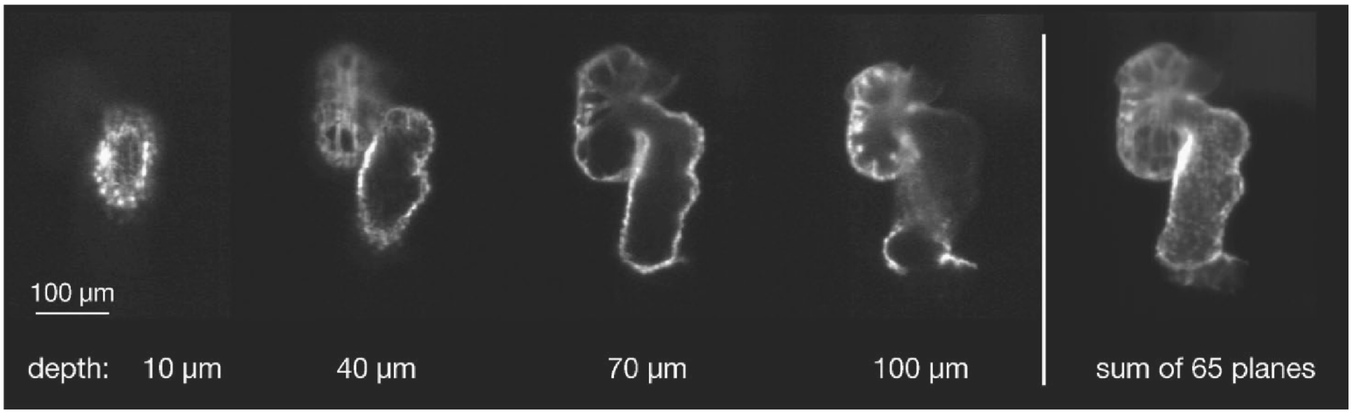

FIGURE 34.11. GFP expression in the developing heart of Medaka imaged by SPIM. Optical sectioning of Medaka heart tube can be performed because fluorescent signal is only emitted from the plane illuminated by of the light sheet. This series of images demonstrates the axial resolving capabilities of SPIM. Each image is separated by 30 µm along the imaging axis. The three-dimensional reconstruction is very good with no out-of-focus data confounding the image.

MICRO-COMPUTERIZED TOMOGRAPHY IMAGING

The recent introduction of commercial ultra-high-resolution laboratory micro-computerized tomography (micro-CT) scanners has revolutionized our ability to non-invasively examine tissues and organs in living experimental animal models, including mice, at spatial resolutions of less than 20 microns. In a 3D sense, this makes it possible to image a 1 µL volume *in vivo*. Several excellent reviews have recently appeared that discuss in detail the physical differences as well as the advantages and limitations associated with each type of small animal imaging system, including micro-CT (Paulus *et al.*, 2000, 2001; Holdsworth *et al.*, 2002).

Operating Principle

The general principles of micro-CT are similar to those used in clinical CT scanners. Most clinical systems consist of a high-power X-ray point source, between 1 and 64 rows of detector elements, and a mechanical gantry that rotates around the patient over a period of minutes [Fig. 34.12(A)]. X rays emitted by the source are collimated into a fan-shaped beam, oriented perpendicular to the rotation axis passing through the patient. Most of the X rays not absorbed by the patient are detected by the detector rows.

Contrast and Dose

The relationship between the X-ray flux emitted by the source, φ_0 and the detected flux, φ, is given by the expression

$$\phi = \phi_o \exp\left(-\int_l \mu_x dx\right)$$

where μ_x is the spatially-varying X-ray attenuation coefficient of the tissue and l is the path of the X rays. This expression may be solved to determine the line integral of the attenuation coefficient to yield

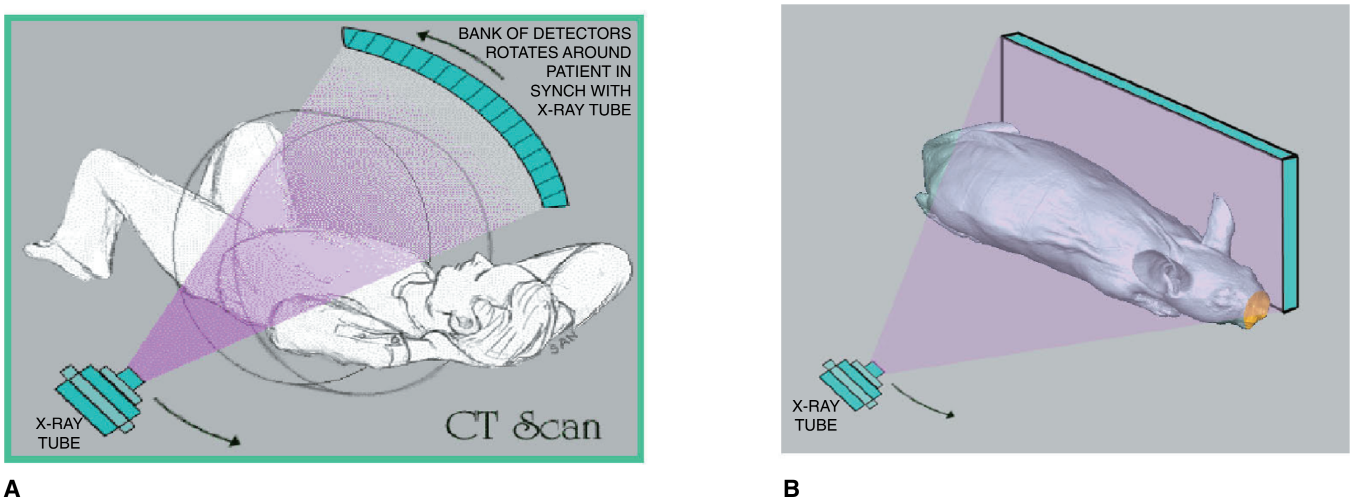

FIGURE 34.12. (A) Layout of a CT scanner showing orientation of body, X-ray source, and detector for a hospital scanner (A) that collimates the X rays into a fan-shaped beam with the long axis parallel to the rotation axis and (B) a micro-CT that uses a cone-shaped X-ray beam and a large 2D X-ray detector that is slightly larger than the mouse and has an effective pixel size of 25 to 40 µm. The detector counts about 50% of the X-ray photons striking it (depending on kilovolts) and X rays passing through the body of the mouse are usually digitized to 10-bit accuracy (12- to 14-bits overall). The distance from the source to the rotation axis is variable from about 5 to 30 cm; shorter spacing gives shorter exposure times but lower MTF and more complex computations.

$$\int_l \mu_x dx = \ln\left(\frac{\phi_o}{\phi}\right)$$

Tomographic image reconstruction is the process of using a number of these integral expressions to calculate values for *m* in a 2D slice or 3D volume. The calculated values for the attenuation produced by each voxel are typically normalized to the attenuation coefficient of water and scaled following the expression

$$CT\ Number = \frac{\mu - \mu_{H_2O}}{\mu_{H_2O}} \times 1000.$$

Although the scaled attenuation coefficient is actually unitless, the reported values are typically cited in pseudo-units of *CT Numbers* or *Hounsfield Units*. Of course, like any other imaging system that relies on the detection of photons, micro-CT is limited by the Poisson noise associated with actually detecting the signal. However, simple calculations relating visibility to contrast and detected signal levels (such as those in Chapters 4 and 8, *this volume*) are complicated by the fact that the imaging algorithms extract 3D information from an entire series of between 90 and 360 2D projection images.

Micro-CT systems typically have poorer contrast resolution than clinical systems. The combination of small detector elements and low X-ray flux leads to signal-to-noise ratios in micro-CT systems that are typically an order of magnitude lower than those of their clinical counterparts. Signal-to-noise ratios can be improved by either increasing the detector element size (at the expense of resolution) or by increasing the number of X rays collected (at the expense of scan time and the dose to the animal).

As in other imaging modalities, the ability to discern structure depends on the contrast of the structure. Generally speaking, contrast in the raw data from the 2D X-ray detector goes down as the overall thickness of the object increases, and goes up as the attenuation of a feature varies from that of its surroundings (as measured in Hounsfield units). In the micro-CT, the kilovolts applied to the X-ray source changes both the peak and the average energy of the X rays emitted: higher energy X rays are more likely to penetrate through the mouse but usually show less differential attenuation (i.e., raw contrast). In theory, information about features with low contrast (soft tissue), will be maximized if about 60% of the X rays are absorbed in the mouse and the remaining 40% detected by the detector. In practice, much mouse work is done with the X ray source operating at ~80 kV (range, 40–100 kV), with the beam filtered through about 0.5 mm of Al to remove very low energy photons that can't penetrate the mouse but can cause damage.

In general, micro-CT scanners only have sufficient contrast resolution to differentiate between different soft tissue types after radio-opaque contrast agents have been added. Figure 34.13 illustrates the use of these compounds in micro-CT animal studies.

Computed Tomography Scanning Systems

Even the largest multi-detector row (multi-slice) clinical X-ray CT systems image only a slice of tissue a few centimeters thick in a single rotation. To image a larger volume, the X-ray source and detector rotate through multiple orbits as the patient bed moves linearly through the gantry. This process of acquiring volumetric image data by translating the patient through the imaging path of a continuously rotating X-ray source and detector is called spiral CT, and is now the dominant clinical method for acquiring volumetric CT data.

In contrast, most preclinical micro-CT systems [Fig. 34.12(B)] employ a large area detector, sized to detect X-rays illuminating much of the test subject in a single exposure. The X-ray source is uncollimated, generating a cone beam rather than a fan beam as in a clinical system. X-ray data is typically collected as a series of 90 to 720 discrete exposures (i.e., step-and-shoot acquisition), and the entire image volume is often acquired in a single orbit acquisition rather than in a multi-orbit spiral acquisition. The bed does not move during the acquisition.

The motivation for using a cone beam configuration for high-resolution micro-CT studies stems from the requirement for a very

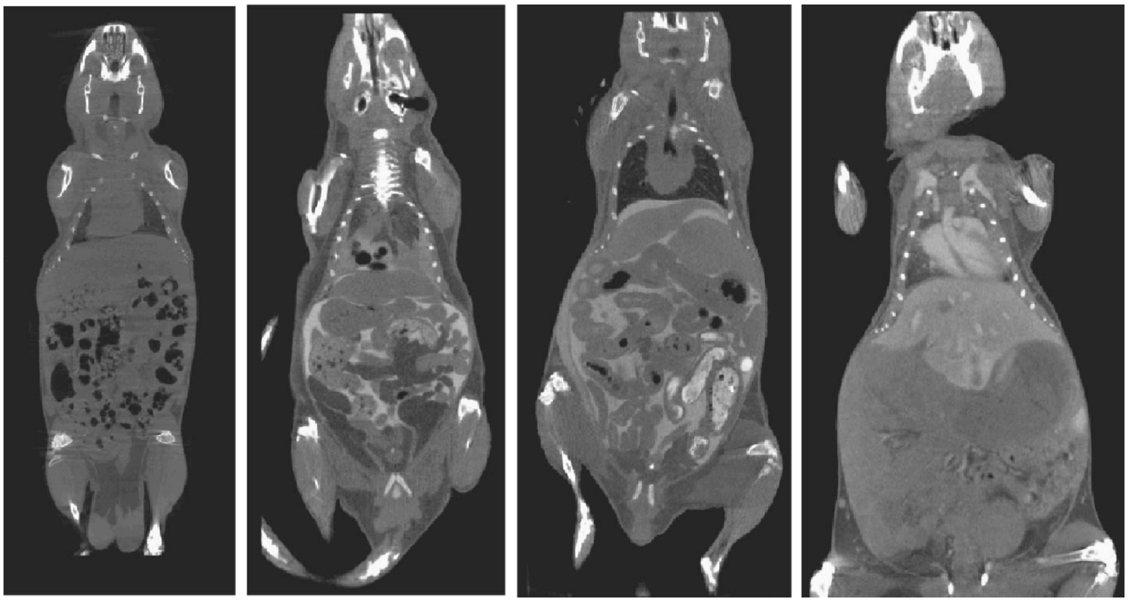

FIGURE 34.13. Micro-CT images of mice with (A) no contrast media, (B) intraperitoneally injected water-soluble contrast medium, (C) intraperitoneally injected water-soluble and oral contrast medium, and (D) blood pool and hepatophillic contrast media. (Images courtesy of CTI/Concorde Microsystems, LLC, Knoxville, TN.)

small (10–15 µm focal spot) microfocus X-ray source. The small focal spot is required to achieve the <50 µm resolution required for most laboratory animal imaging studies. Microfocus X-ray sources operate at very low power, typically less than 100 W, and consequently generate several orders of magnitude lower X-ray flux intensities than their clinical counterparts. In order to make efficient use of the available X rays, the clinical fan beam is expanded into a cone beam, leading to the scanner geometry described above.

The 2D micro-CT detector is typically a large format CCD camera which collects images appearing on a high-resolution phosphor screen. The phosphor screen images are transferred to the CCD by either a conventional lens or a fiber-optic array.

Micro-CT scanners are intrinsically high-resolution devices. Available X-ray sources can have a focal spot size of <10 µm and detector pixel sizes range from 10 to 40 µm. With these components, volumetric image resolutions on the order of 10 µm are readily achievable but only at the cost of either being restricted to imaging high-contrast structures, such as bone, or exposing the mouse to dangerous levels of X-ray radiation. A typical high-resolution micro-CT image of a mouse femur is shown in Figure 34.14.

When seeking to enhance micro-CT contrast/resolution, X-ray dose is an important consideration. A typical micro-CT study with ~100 µm spatial resolution and sufficient contrast resolution to differentiate between bone, soft tissue, and fat exposes a mouse to approximately 5 to 10 cGy. This is below the dose expected to produce chronic or acute physiological responses in mice (~20 cGy). As the spatial and contrast resolution are increased, some physiological effects may be expected and in the limit, the typical LD 50/30 of 7 Gy may be approached. Figure 34.15 shows the approximate dose/resolution trade-off for studies designed to image only bones (2500 HU contrast resolution); to separate bones, soft tissue, and fat (100 HU contrast resolution); and for studies designed to differentiate between soft tissues (5 HU contrast resolution). Based on this chart, if one sets an exposure limit to 10 cGy, it is possible to image bone at a resolution of 20 µm; separate bone, soft tissue, and fat at a resolution of 100 µm and to differentiate between soft tissue organs at a resolution of 400 µm without causing harm to the animal.

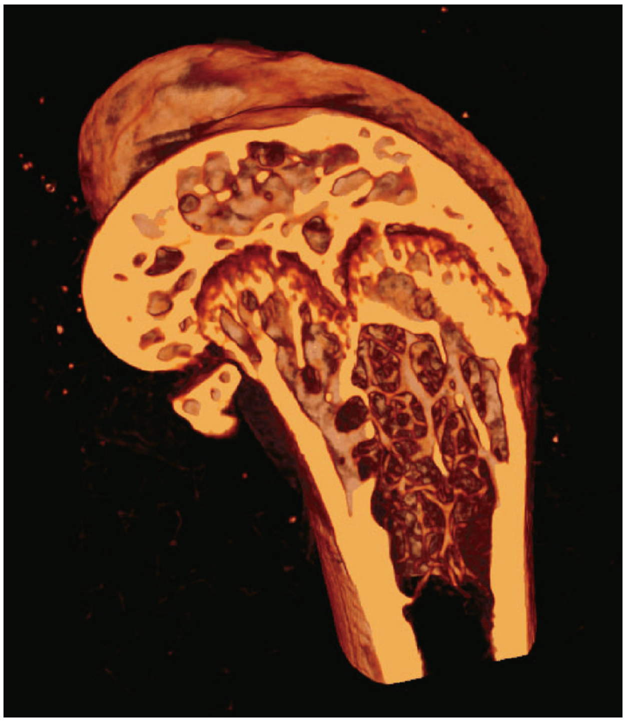

FIGURE 34.14. High resolution micro-CT image of a mouse femur. Field width, 4 mm. (Image courtesy of CTI/Concorde Microsystems, LLC, Knoxville, TN.)

In the recent past, the resolution, image quality, and scan times of micro-CT have increased substantially, chiefly because of

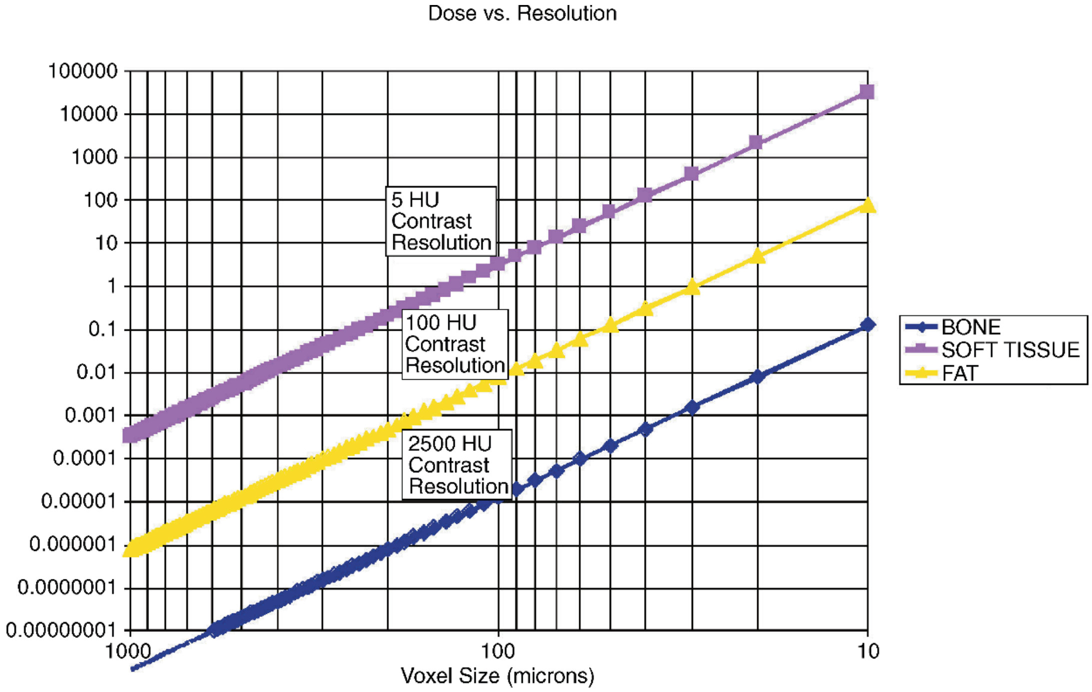

FIGURE 34.15. Approximate relationship between resolution and dose for micro-CT studies as a function of required contrast resolution. (Chart courtesy of CTI/Concorde Microsystems, LLC, Knoxville, TN.)

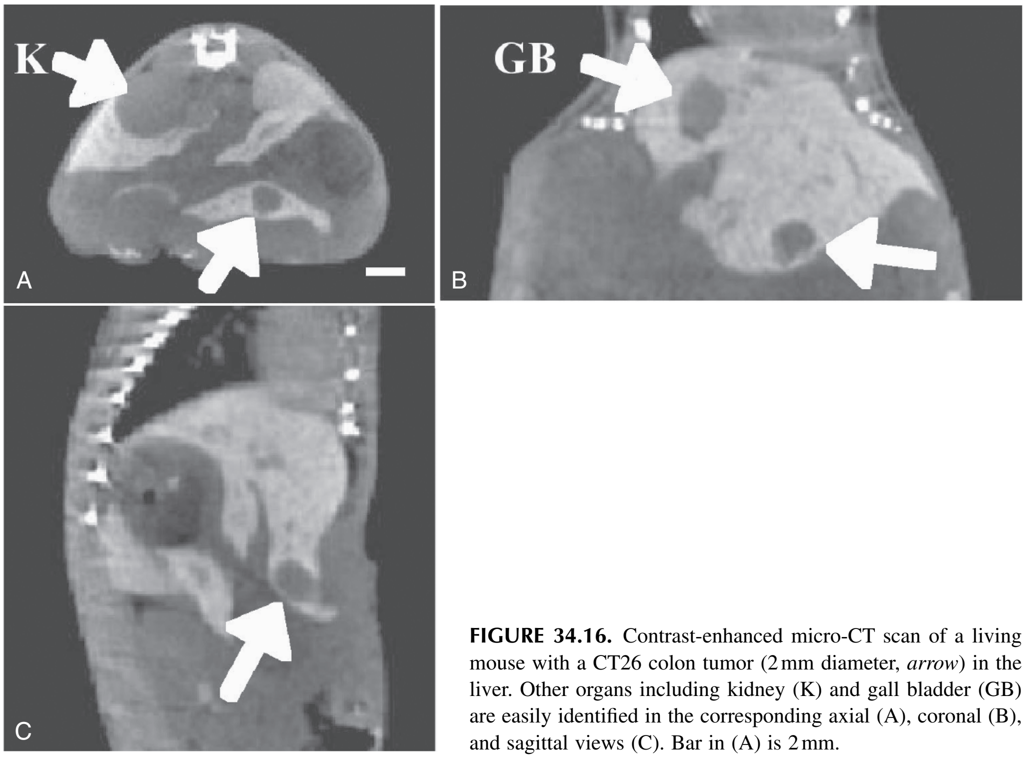

FIGURE 34.16. Contrast-enhanced micro-CT scan of a living mouse with a CT26 colon tumor (2 mm diameter, *arrow*) in the liver. Other organs including kidney (K) and gall bladder (GB) are easily identified in the corresponding axial (A), coronal (B), and sagittal views (C). Bar in (A) is 2 mm.

improvements in 2D CCD X-ray detectors and the algorithms used to reconstruct the image data. The main areas in which additional improvements can be expected include the development of new iterative reconstruction algorithms and higher power microfocus X-ray sources. Should both these succeed, whole animal scan times of a few seconds may be achieved and high-resolution, high-contrast images may be generated at significantly reduced doses.

Although micro-CT scanning of bones and skeletal features produces outstanding images due to the inherently high density of these tissues, success in imaging native soft-tissue structures has thus far been modest at best. As mentioned above, soft tissue contrast can be enhanced in clinical CT with the use of non-targeted, water-soluble radiographic contrast agents such as iohexol. These agents are non-specific in that they are not designed to target any particular tissue. The contrast agents used on clinical CT scanners are not suitable for use with research micro-CT scanners because they rapidly undergo renal elimination and localize in the urinary bladder within a few minutes of injection. This pharmacodynamic mismatch between the agent lifetime and the relatively long data acquisition times associated with micro-CT precludes their use. Recently however, tissue-specific agents suitable for use in micro-CT have significantly extended the usefulness of this non-invasive imaging technique, allowing exquisite vascular and soft tissue images to be made in living mice (Figs. 34.16 and 34.17; Weichert, 2004). Moreover, it is now possible to non-invasively perform virtual serial colonoscopy in mouse colon cancer models (Pickhardt *et al.*, 2005). This finding is paramount in drug development because it is now possible to non-invasively monitor the effectiveness of anticancer agents over time in living mouse tumor models. Finally, although *in vitro* systems are currently capable of sub-10 μm spatial resolution, these systems are typically only used for imaging non-living tissue specimens due to the long acquisition time requirements and associated radiation dose. While *in vivo* scanners are certainly capable of obtaining sub-20 μm spatial

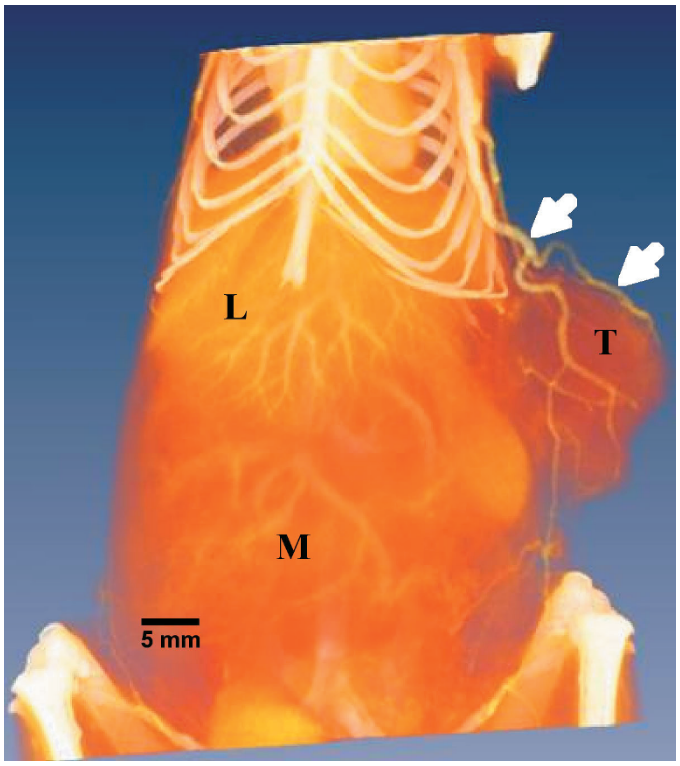

FIGURE 34.17. Three-dimensional volume-rendered micro-CT image of a Colon-51 tumor-bearing live mouse, showing tumor vasculature contrast enhanced using a blood pool agent developed by Weichert and now being marketed as Fenestra VC (Alerion Biomedical, San Diego, CA). Tumor (T) feeder vessels are easily visible (*arrows*) with the aid of this contrast agent. The heart is visible within the rib cage and exquisite vascular details are also visible in the liver (L) and mesentary (M).

resolution, absorbed radiation dose becomes a concern due to increased scan times. Using appropriate long-acting contrast agents, exquisite micro-CT images can be obtained from soft tissues and tumors in live mice at 90 to 100 µm without harming the animal. In our hands, we have performed serial imaging studies at this resolution in the same mice over several weeks with no apparent harm to the animals.

Technological enhancements have truly revolutionized small animal imaging capabilities within the past several years alone. It is now possible to generate spectacular anatomic images at ultra-high resolution in living animals by micro-CT. Although this affords anatomic information, the recent introduction of hybrid microscanners, including a micro-CT/micro-SPECT hybrid, will significantly extend our capabilities to non-invasively garner both anatomic and biochemical information simultaneously with the use of molecular imaging agents.

MAGNETIC RESONANCE MICROSCOPY

Magnetic resonance imaging (MRI) is very well established as a non-invasive diagnostic technique in human medicine with particular strength in visualizing soft tissue. In comparison to a typical clinical MRI with spatial resolution on the order of 1 mm, magnetic resonance microscopy (MRM) can be broadly defined as MRI with a spatial resolution less than 100 microns.

MRM applications are dominated by *in vivo* and *ex vivo* structural biological imaging, concentrated almost exclusively on mapping water and mobile lipid distributions in soft tissues. MRM is unfettered by the optical opacity of a material, and is particularly suited to absolute measurements of mass transport and flow that cannot be obtained by optical methods. However, MRM is hindered by a low intrinsic sensitivity, which ultimately limits spatial and temporal resolution to significantly more modest values than can be achieved with optical techniques.

Basic Principles of Nuclear Magnetic Resonance

MRM relies on nuclear magnetic resonance (NMR) as a source of spatially resolvable signal. NMR is a phenomenon observed when nuclei possessing a non-zero nuclear spin, and therefore a magnetic moment, are placed in a strong magnetic field and excited away from equilibrium with radiofrequency energy [Fig. 34.18(B)]. The most common biologically-abundant nuclei targeted by NMR and MRI include ^{1}H, ^{13}C, ^{23}Na, and ^{31}P. ^{19}F is also used as an NMR/MRI label due to its low natural biological abundance. The magnetic field polarizes the population of nuclear dipoles according to quantum mechanical rules, generating a bulk nuclear paramagnetism within a sample [Fig. 34.8(A)].

At equilibrium, the bulk magnetization is aligned parallel to the polarizing magnetic field and is undetectable. The magnetization becomes detectable following excitation by a radiofrequency pulse at a specific frequency, f, determined by the Larmor equation

$$f = \frac{\gamma}{2\pi} B \tag{1}$$

where B is magnetic flux density in Tesla, and γ is the gyromagnetic ratio for a given nucleus in rad/s/T. For example, $y/2\pi$ for the ^{1}H nucleus is approximately 42 MHz/T, so for a magnetic field strength of 7.0 T, the Larmor or resonance frequency is close to 300 MHz. The excited bulk magnetization has a component per-

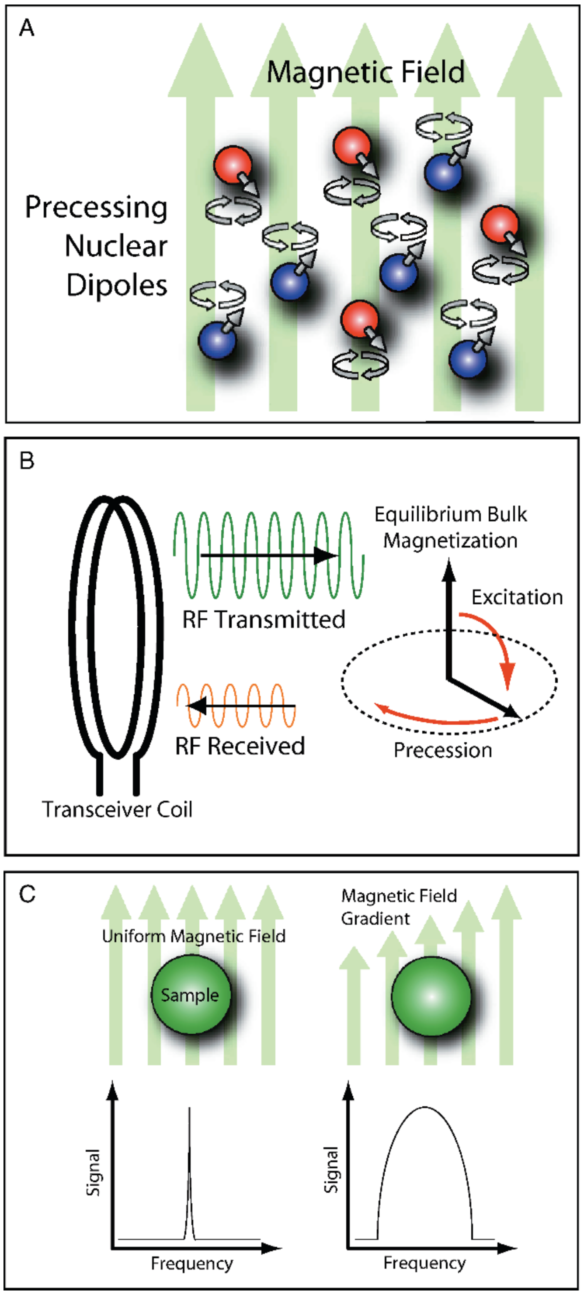

FIGURE 34.18. Basic principles of magnetic resonance microscopy. (A) A strong magnetic field polarizes the population of nuclear dipoles within a material. In this case a spin-1/2 nucleus is shown, which can adopt only one of two energy states (red and blue nuclei) in the magnetic field. The dipoles precess around the applied field at the Larmor frequency (see text). The slight excess of dipoles aligned with the field in the low energy state (typically 10–100 ppm) leads to a bulk nuclear paramagnetism. (B) A radiofrequency pulse at the Larmor frequency excites the bulk nuclear magnetization away from equilibrium. Once excited, the bulk magnetization precesses at the Larmor frequency and induces a small voltage in the transceiver coil which decays as the nuclear spin system returns to equilibrium. (C) In a uniform magnetic field (above left) there is no spatial variation in resonance frequency as seen in the spectrum for a water sample (below left). Application of a magnetic field gradient (above right) encodes spatial position in the precessional frequency of the spin system. Fourier analysis of the frequency and phase of the detected signal allows the spatial distribution of spins in the gradient direction to be reconstructed as a 1D projection of the sample (below right). Additional pulsed gradients in orthogonal directions allow 2D and 3D image formation (not shown).

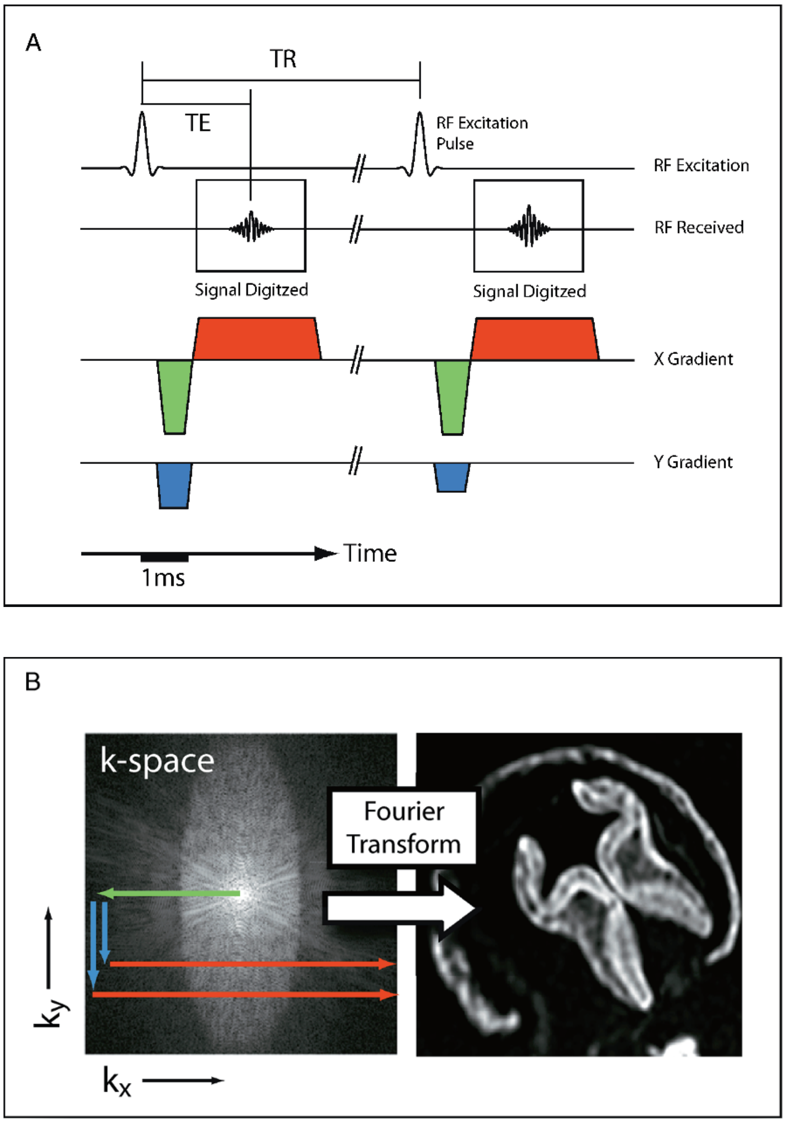

FIGURE 34.19. (A) Simplified schematic of a magnetic resonance imaging pulse sequence with the gradient pulses associated with slice selection omitted for clarity. Two excitation pulses are shown separated by a repetition time (TR) in the range 10 ms to 10 s. The time between the excitation pulse and the signal echo (TE) is in the 1 ms to 50 ms range for high-field microscopy. The 1 ms time bar is a representative reference only. (B) Following the RF excitation pulse, all ^{1}H nuclear spins are at the center of *k*-space: $(k_x, k_y) = (0, 0)$. The negative *x*-gradient (*green*) and *y*-gradient (*blue*) pulses are played out simultaneously and move the spin system in *k*-space as shown. The positive *x*-gradient pulse (*red*) is then played out and the spin-system moves in the k_x direction at a fixed k_y coordinate (*lower red line*). During this gradient pulse, the received signal from the sample is digitized and saved to a 2D data array. This process is then repeated as the amplitude of the blue pulse is changed to sweep data acquisition across *k*-space (*upper red line*). The final spatial resolution of the real-space image is determined by the maximum *k* coordinate reached in each dimension. Conversely, the field of view of the final image is determined by the digitized sampling interval in *k*-space. Following a complete traverse of the required region of *k*-space, the final real-space image is reconstructed using a 2D Fourier transform. In practice, phase-sensitive quadrature detection of the received signal is equated to the real and imaginary parts of *k*-space required for the Fourier transform. The complex image resulting from Fourier transformation is then converted to a magnitude image for display purposes.

pendicular to the polarizing field (the transverse component) and precesses around the field direction at the Larmor frequency, a process that induces a detectable voltage in an appropriately-placed receiver coil [Fig. 34.19(B)].

Following excitation, the precessing transverse component decays or relaxes exponentially with a time constant, T_2. Simultaneously, the magnetization component parallel to the main field relaxes back to its equilibrium value with a time constant, T_1. Typical relaxation times for liquid water in tissues range from milliseconds to seconds with T_1 always greater than T_2. Consequently, the natural resonance line-widths in NMR fall in the 1 Hz to 1 kHz range and are therefore extremely narrow when compared with the Larmor resonance frequency.

Magnetic Resonance Image Formation

Unlike most other imaging modalities, MRM does not physically "scan" real space because the wavelength of the radiofrequency radiation involved is typically much larger than the length-scale of the sample (extreme near field). It turns out instead, that the Larmor Eq. (1) can be exploited to spatially resolve the NMR signal. If we arrange for the magnetic field to vary linearly across a sample, then the resonance frequency becomes proportional to distance along the gradient direction (frequency encoding). In the following description of MR image formation, we will assume that the sample contains only water (singlet resonance) and that other parameters such as relaxation, diffusion, motion, etc., can be ignored. At this point it is worth looking at how the phase of the NMR signal varies with time in a field gradient that may also vary with time. In one dimension, with the gradient along the *x*-axis, we have

$$\begin{aligned}\phi(x,t) &= \int_0^t dt'\omega(x,t') \\ &= \int_0^t dt'\gamma B(x,t') \\ &= \int_0^t dt'\gamma G_x(t')x \qquad (2)\end{aligned}$$

where $G_x(t)$ is a time-varying magnetic field gradient (in *T*/*m*) and x is the position of a water molecule (spin) in the gradient direction, ignoring diffusion and bulk motion. We can define a new variable, $k_x(t)$, the significance of which will become apparent, as

$$k_x(t) = \int_0^t dt'\gamma G_x(t') \qquad (3)$$

The time-varying signal arising from water at a given position in the gradient can be expressed, using Eqs. 2 and 3, as

$$\begin{aligned} S(x,t) &= \rho(x)e^{i\phi(x,t)} \\ &= \rho(x)e^{ik_x(t)x} \end{aligned} \qquad \textbf{(4)}$$

where $\rho(x)$ is the so-called proton density which is proportional to ^{1}H nucleus concentration. Additional terms describing the effects of relaxation, motion, and RF-pulse-sequence timing are omitted here for simplicity. This expression in turn leads to the total signal detected from a sample as a function of k_x

$$S_{tot}(k_x) = \int_{-\infty}^{\infty} dx \rho(x)e^{ik_x x} \qquad \textbf{(5)}$$

which is the inverse Fourier transform of the proton density in x. k_x can be thought of as a spatial frequency of the proton signal, with units of m^{-1} (as opposed to s^{-1} for temporal frequency) and is the coordinate for the one-dimensional (1D) Fourier inverse-space of x. This expression is easily extended to three dimensions

$$S_{tot}\left(k_x, k_y, k_z\right) = \int_{-\infty}^{\infty} dx \int_{-\infty}^{\infty} dy \int_{-\infty}^{\infty} dz\, \rho(x, y, z)e^{i\left(k_x x + k_y y + k_z z\right)}$$

with $\rho(x,y,z)$ being the sought-for image. All positions in real space only occupy one position in k-space at a given time, so an MR image must be acquired by scanning k-space, then Fourier transforming the resulting inverse-space image to reconstruct the real-space image (Fig. 34.19). From Eq. 3 we can see that the sample can be moved in k-space by applying appropriate sequences of time-varying field gradients to traverse k-space in one or more dimensions. An example k-space trajectory for the gradient echo imaging sequence is detailed in Figure 34.19. Digital signal acquisition can take place continuously or discontinuously during only specific parts of the k-space trajectory. The most common k-space scanning trajectory involves acquiring one line of data in k_x (with k_y and k_z fixed) per radiofrequency (RF) excitation pulse. Rapid scanning can be achieved by scanning larger regions of k-space per excitation pulse, as is the case for the echo-planar imaging (EPI) sequence 1. Finally, the real-space image, $\rho(x,y,z)$, is reconstructed by Fourier transformation of the scanned k-space data.

The deviation in the Larmor frequency brought about by the field gradient creates a frequency difference across a sample of between 10 kHz and 1 MHz in conventional liquid-state MRM. A single line of k-space is acquired in milliseconds, with a whole plane of k-space traversed in anything from tens of milliseconds to minutes depending on the pulse sequence employed. Signal averaging is achieved by simple repetition of a trajectory segment. The RF excitation pulse resets the k-space.

The complement of frequency-encoded signal detection is frequency selective excitation. Here a magnetic field gradient is applied in conjunction with an amplitude-modulated (and in some cases) phase-modulated RF pulse (Fig. 34.20). The modulation of

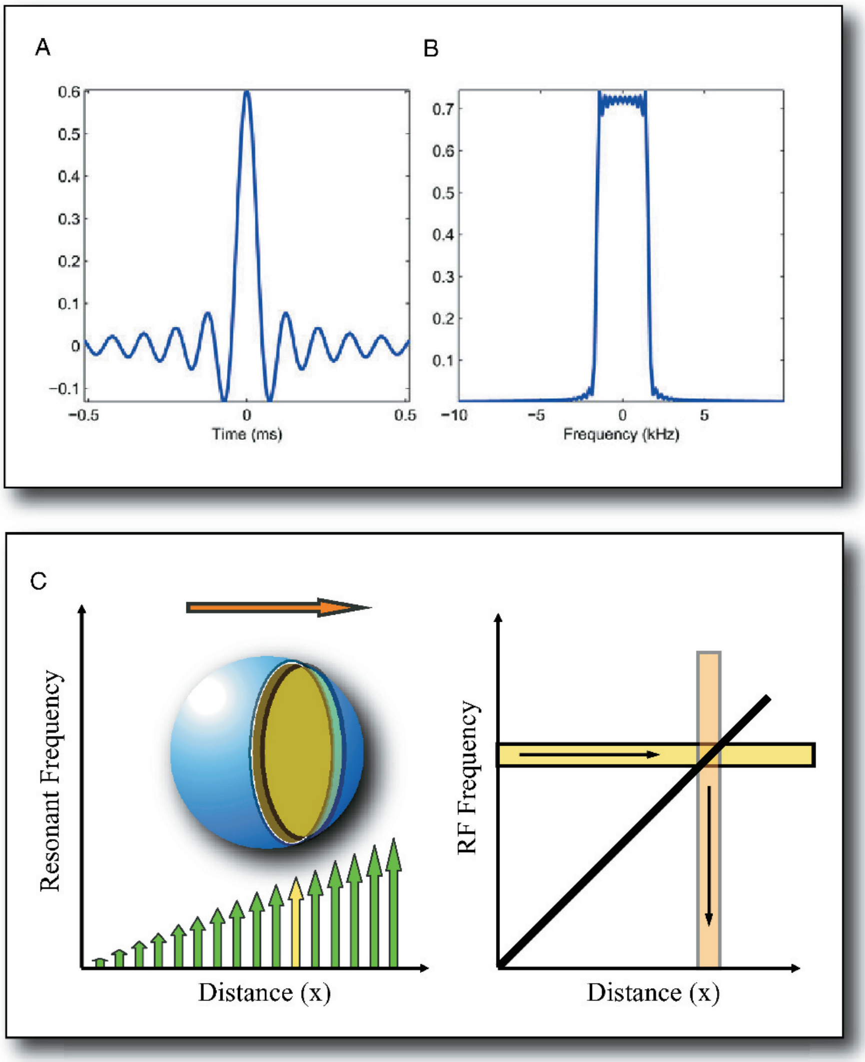

FIGURE 34.20. An amplitude modulation waveform for the RF carrier at the Larmor frequency (A) produces a band-limited excitation of the nuclear spins (B). If such an RF waveform is used in combination with a linear magnetic field gradient, then only a limited slice or slab will be excited perpendicular to the gradient direction. Three such slice-selective pulses could be combined to limit excitation to a cubic sub-volume within a sample.

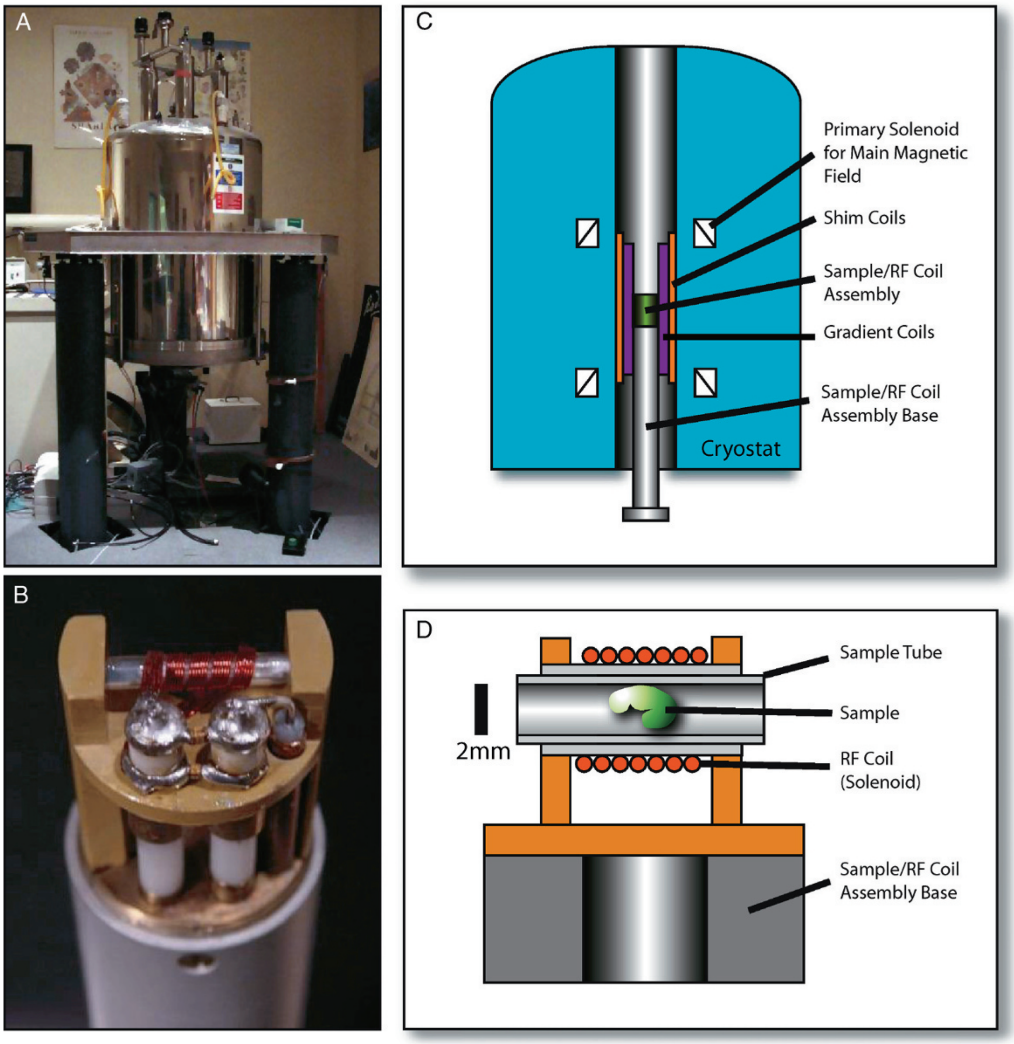

FIGURE 34.21. A typical MRM hardware configuration: (A) an 11.7 Tesla vertical bore superconducting magnet. This hardware is identical to that used for high-resolution NMR spectroscopy. (B) Three millimeter transverse RF solenoid (copper winding at upper center) and tuning circuitry for excitation and detection of the MR signal. (C) Simplified schematic cross-section of a vertical bore MRM setup. The gradient and shim coils are secured within the magnet bore and the RF coil/sample assembly introduced for each experiment. (D) Enlargement of a transverse configuration for the solenoidal RF coil and sample tube. The sample is often surrounded by a suitable fluid, such as buffered saline or culture medium. For fixed samples where background signal needs to be eliminated, the sample can be surrounded by ^{1}H-free, fluorinated fluids. Environmental control can be provided by thermostatically controlled airflow through the bore of the coil/sample assembly base.

the carrier frequency of the excitation pulse limits the frequency content, so that the excitation becomes spatially limited in the presence of a field gradient. For example, a 1 ms shaped pulse might have a bandwidth of 4 kHz that, in the presence of a 10 mT/m field gradient would limit NMR excitation to a region approximately 1 cm wide in the gradient direction, but would be unlimited perpendicular to the gradient direction. This process is termed slice or slab selection and can be extended to line and volume selections by using multiple, selective RF pulse/gradient combinations. Slice selection is often used for *in vivo* imaging where interleaved acquisition of multiple 2D k_{xy}-spaces separated in z is more time-efficient than scanning the complete 3D k_{xyz}-space.

In a typical MRM experiment, a sample, such as an anesthetized mouse or a fixed embryo, is secured within an appropriate holder and placed within the RF coil. Additional physiological monitoring, anesthesia lines, and environmental control are often integrated into the RF coils/sample assembly. The gradient and shim coils are normally secured more permanently within the main magnet bore (Fig. 34.21) requiring only the RF coil and sample to be introduced for each experiment. The RF coil/sample assembly is then placed at the center of the main field and gradient coils for imaging. The shim coil currents are adjusted to minimize magnetic inhomogeneities in the sample, the synthesizer frequency set to the Larmor frequency determined from the received signal and the strength of the RF excitation pulses calibrated. The duration of an image acquisition may vary from less than a second to more than a day and is largely determined by the required spatial resolution and signal-to-noise ratio. The RF power deposition in the sample varies widely with pulse sequence design and has the potential to cause significant heating. Changes to the pulse sequence timing and RF pulse waveform specifications can minimize peak and average power deposition. Heating effects increase rapidly with the Larmor frequency (increasing field strength) and power deposition can be estimated, monitored and controlled for *in vivo* imaging studies.

Magnetic Resonance Microscopy Hardware

The hardware for MRM consists of three major components and their associated electronics: (1) a permanent or electromagnet that generates the main polarizing field, (2) one or more radiofrequency coils for excitation and signal detection, and (3) a three-axis set of magnetic-field-gradient coils. The sample is placed within the RF coil which in turn is placed within the gradient and the main solenoid. The main, polarizing field is typically generated by a cryogenically-cooled, superconducting electromagnet, although permanent magnets and even resistive electromagnets are in use. The uniformity or homogeneity of the polarizing field plays a critical role in successful high-quality MRM. Additional room-temperature field correction or shim coils are routinely used to improve the fundamental homogeneity of the magnetic field within the imaging volume. RF coils for MRM are most commonly simple loops, solenoidal resonators, or a volume resonator design called a birdcage. A single coil may be used for both transmission/excitation and reception, or a larger transmitting volume coil with good RF field homogeneity can be used with a high-sensitivity receiver loop coil (surface coil).

The RF power absorbed by a sample during imaging varies widely with the type of pulse sequence employed. Some sequences involve rapid RF pulsing at relatively high power which ultimately will lead to tissue heating. Power deposition also increases rapidly with field strength for a given pulse sequence.

The signal received from the RF coil is amplified by a low noise preamplifier prior to demodulation from the Larmor frequency (see sidebar) and digitized at rates from about 100 kS/s to 2 MS/s. Raw *k*-space data is reconstructed and displayed by the operating-console computer.

The coils generating magnetic field gradients (gradient coils) are usually wound on a cylindrical former within the main magnet bore. The coil windings are designed to produce independent, linear field gradients over the imaging volume in each of the three cardinal directions (x, y, z). The maximum gradient strengths required for MRM typically exceed 500 mT/m and may rise to more than 5 T/m in high-performance hardware. Even at these strengths, the maximum field perturbation from the gradient coils rarely exceeds 1% of the main magnetic field.

A functional MRM system requires a high-stability, high-accuracy frequency synthesizer that provides the reference oscillation for both RF transmission and reception. Amplifiers for the RF and gradient coils are controlled by a pulse sequencer that in turn is coordinated by the operating-console computer.

Strengths and Limitations of Magnetic Resonance Microscopy

Whereas magnetic resonance imaging of humans is very well established as a medical diagnostic tool, microscopy has developed at a slower rate. MRM cannot compete with optical microscopy in terms of spatial resolution and sensitivity, but has several unique strengths that benefit certain applications. Specifically, MRM is not limited by the opacity of an object to light, because it employs radiofrequency radiation with wavelengths much larger than the typical sample size.

Optimizing MRM is a complex trade-off between acceptable signal-to-noise ratio, temporal resolution, and spatial resolution. The NMR experiment has an intrinsically low sensitivity, so requirements for minimum SNR tend to place lower bounds on spatial and temporal resolution. Consequently, acquiring high spatial resolution MRM with voxel sizes in the 10 to 100 micron range typically requires tens of minutes to hours to achieve an acceptable SNR.

Various estimates place the ultimate limit for MRM spatial resolution in the neighborhood of 1 μm for liquid water at room or physiological temperatures.[1] These estimates consider the effects of molecular diffusion, T_2 relaxation, microscopic field inhomogeneity, and sensitivity (Callaghan, 1991). Other factors, including hardware design and sample size, lead to practical MRM isotropic resolution limits greater than 10 μm. The achievable spatial resolution is limited by sensitivity factors, specifically the signal-to-noise ratio achievable in a given acquisition time.

As a general rule, high-resolution MRM with spatial resolutions less than 100 μm benefits from the use of polarizing magnetic fields greater than 3 Tesla, sometimes as high as 17.5 Tesla. Although this leads to a greater nuclear paramagnetic polarization, other factors such as increasing T_1 relaxation times, decreasing T_2 relaxation times, and increased susceptibility-based field inhomogeneities tend to diminish the expected gains in sensitivity and signal-to-noise ratio efficiency.

High-performance gradient hardware, with higher maximum amplitudes (*T/m*) and faster slew rates (*T/m/s*) are almost always an advantage in MRM. Microscopy gradients capable of 10 *T/m* allow high spatial and temporal resolution imaging of small samples.

Another approach to increasing the sensitivity of MRM is through RF coil design. Various groups have developed microcoils with dimensions smaller than 1mm to boost sensitivity in very small samples. Some of the highest resolution MRM images obtained have employed such designs (Grant *et al*., 2001; Lee *et al*., 2001; Ciobanu and Pennington, 2004).

Image Contrast in Magnetic Resonance Microscopy

Signal differences between tissues in ^{1}H MRM of biological samples largely arise from differences in the microscopic environment of intracellular and interstitial water. Chemical differences between molecules containing ^{1}H nuclei also contribute to image contrast, for example, between water and lipid-rich tissues. Parameters influencing MRM image contrast include T_1 and T_2 relaxation times, NMR nucleus concentration, temperature, diffusion coefficient, fluid velocity, magnetic susceptibility, and magnetization transfer coefficients of a material. The influence that each of these parameters has on image contrast can be accentuated or suppressed by careful design of the sequence of radiofrequency and field gradient pulses played out prior to signal acquisition. For example, specific pulse sequence designs allow the time delay between excitation and signal acquisition to be increased, accentuating differences in the T_2 relaxation time of materials. Reducing the time delay between excitation pulses accentuates short T_1 materials that appear brighter in such images.

Motion of water and other fluids can be encoded in the phase or amplitude of MRM images using gradient pulse combinations. Both coherent motion (flow) and incoherent motion (diffusion) can be quantified by MRM over a 2D plane or 3D volume of an optically opaque material. MRM measurements of water diffusion within organized tissues have been particularly well developed and are capable of quantifying subresolution ensemble molecular interactions with restrictive or hindering boundaries (Tuch, 2003). For example, diffusion tensor imaging (DTI) maps diffusion

---

[1] About 3 to 4 μm has been obtained on very small specimens (9 Tesla; Ciobanu and Pennington, 2004).

anisotropy within tissues using a simplified model of molecule-boundary interactions (Pierpaoli *et al*., 1996). Diffusion tensor MRM has been applied to brain development in mice (Zhang *et al*., 2003), dysmyelination models (Song *et al*., 2002), and myocardial fiber structure (Jiang *et al*., 2004).

In addition to endogenous image contrasts, such as relaxation time and molecular diffusion, it is possible to introduce exogenous MRM contrast agents that target specific tissues or physiology within a living system. Gadolinium chelates are widely used, both individually and bound to larger molecules, to reduce the T_1 relaxation time of surrounding water (Weinmann *et al*., 1984, 2003). Ionic manganese is a calcium analog and T_1 contrast agent that, at low concentrations, has been used as an *in vivo* trans-synaptic axonal transport tracer (Pautler and Koretsky, 2002; Pautler *et al*., 2003; Aoki *et al*., 2004). Tracking of progenitor, stem, or immune cells using MRM is a recent growth area (Hinds *et al*., 2003; Shapiro *et al*., 2004) typically employing variants of superparamagnetic iron oxide (SPIO) particles as intracellular T_2* contrast agents (Foster-Gareau *et al*., 2003). The development of molecular imaging for MRM, targeting both gene expression and metabolism within a living organism is likely to be the next significant field of investigation (Louie, 2000; Allen, 2004) and holds great promise for future non-invasive biomedical research.

Magnetic Resonance Microscopy Applications

Phenotyping

MRM is widely used for phenotyping genetically manipulated organisms such as transgenic mice (Johnson *et al*., 2002a, 2002b; Lo *et al*., 2003) leading to the development of high throughput techniques for imaging more than one animal simultaneously (Bock *et al*., 2003). MRM brain atlases of adult inbred mouse strains are being constructed by several groups (Kovacevic *et al*., 2005; Segars *et al*., 2004).

Histology

Ex vivo MR histology exploits the lack of physiological motion and extended data acquisition times to generate high-resolution structural images of various organisms (Figs. 34.22 and 34.23) (Johnson *et al*., 1993; Johnson *et al*., 2002a). MRM lacks the spatial resolution and staining flexibility of optical histology, but preserves the 3D structure of tissues and eliminates the need for dehydration, embedding, and physical sectioning and their associated artifacts. As a non-invasive technique, MRM can even precede conventional histology, providing a valuable structural reference for subsequent histological sections.

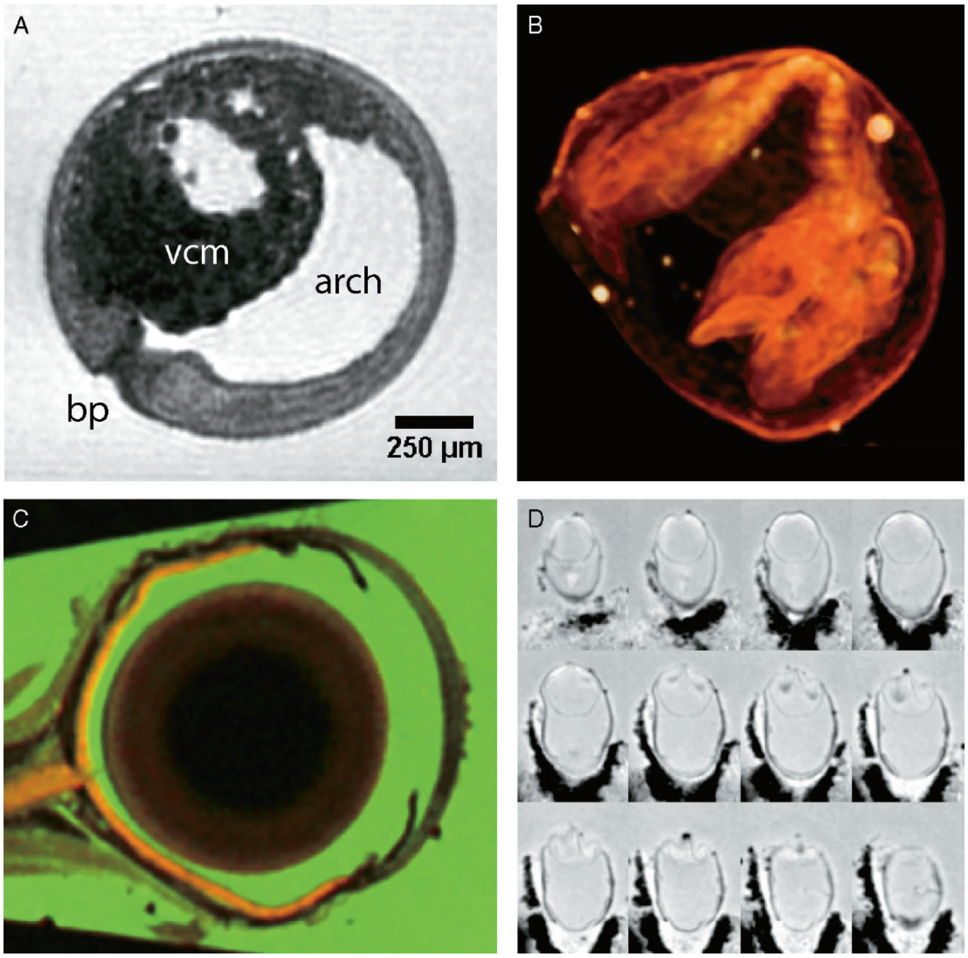

FIGURE 34.22. Examples of MRM histology of biological samples. (A) High-resolution 3D MRM of a fixed late gastrula stage *Xenopus laevis* embryo with a nominal isotropic spatial resolution of 16 microns. The vegetal cell mass (vcm), blastopore (bp), and archenteron (arch) are clearly visualized in this section. (B) Volume texture rendering of a 3D MRM image of a fixed 8.5 dpc mouse embryo within its yolk sac. (C) Central section through a composite MRM image of a fixed mouse eye. The red channel encodes the isotropic-diffusion-weighted image, highlighting regions of restricted diffusion within the chorioretina (*orange*). The green channel encodes the T_2-weighted image in which free-fluid appears bright. The low intensity circular feature within the globe of the eye is the crystalline lens. (D) Montage of sections from a 3D MRM image of a fixed 7 dpc mouse embryo with nominal 20 micron isotropic spatial resolution.

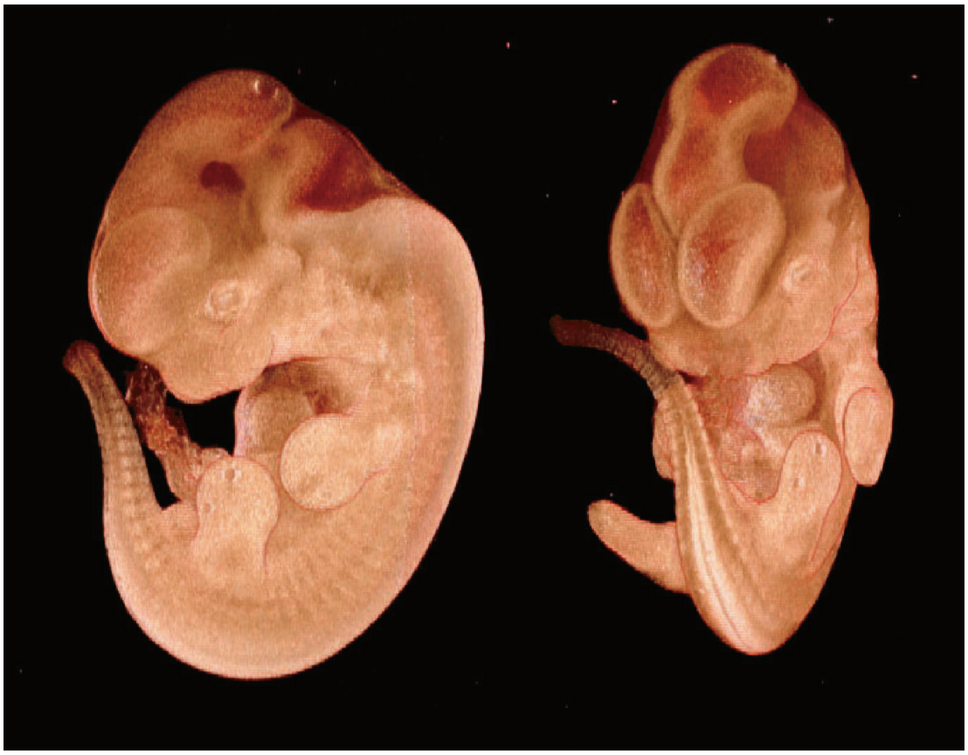

FIGURE 34.23. Volumetric rendering of an 11-day postcoital mouse embryo. Because the sample has not been dehydrated, the global geometric preservation of the embryo is excellent.

Developmental Biology

MRM has been applied to structural imaging of mouse (Jacobs, 1999; Chapon, 2002) and quail embryos and to serial *in vivo* imaging of the *Xenopus laevis* embryo (Papan *et al*., 2001; Jacobs *et al*., 2003). MRM leverages its ability to image optically opaque specimens to generate 3D data which would be difficult or impossible to obtain by other methods. MRM is particularly suited to studies of dynamic developmental processes such as morphogenesis. As for phenotyping, MRM is proving valuable in the construction of reference developmental atlases for mouse, quail, and other embryos that are too large or opaque at later stages for optical imaging (Dhenain *et al*., 2001; Matsuda *et al*., 2003).

Other Applications

MRM is in many ways underexploited outside the realm of vertebrate imaging. MRM is an excellent resource for botanical imaging, exploiting minimal physiological motion to generate high spatial resolution images (Edzes, 1998; Kockenberger, 2001, 2004) and is especially suited to imaging flow and water distribution within plant samples (Kuchenbrod *et al*., 1998). MRM has also seen applications in opaque bioreactors and biofilms, studying local flow and structure beyond the capabilities of optical microscopy (As and Lens, 2001; Paterson-Beedle *et al*., 2001; Manz *et al*., 2003; Seymour *et al*., 2004).

Future Development of Magnetic Resonance Microscopy

The future of MRM is likely to include incremental improvements in spatial resolution and sensitivity as hardware design and fabrication methods are refined. Ironically, clinical MRI has led the way in technical advances, driven by the needs and resources of medical diagnosis and therapy. Some of these technologies, including phased-array RF coils and advanced pulse sequence designs, will be reapplied to MRM applications. However, it is in the development of new molecular imaging agents in model organisms that we will most likely see the greatest advances in MRM in the near future.

CONCLUSION

The imaging modalities discussed in this chapter are emerging tools directed at meeting the growing need for volumetric microscopy of challenging specimens. They join confocal laser-scanning and two-photon laser-scanning microscopy in the suite of microscopic imaging techniques that enable entire, whole-mounted specimens to be studied. Each of these volumetric imaging tools plays an important role in the imaging toolkit, as none answers all needs. SIM/EFIC is a high-resolution method that is capable of capturing the entire volume of large specimens; however, it is inherently destructive as biological samples must be fixed, dehydrated, and embedded, and then must be sectioned. Although imaging the block face avoids the distortions resulting from the sectioning process, the specimen is still subject to any fixation and dehydration artifacts. As presently employed, OPT requires extensive clearing of a specimen to render it translucent, and so is subject to the same fixation and shrinkage artifacts as SIM/EFIC. A major strength of OPT on fixed specimens is its ability to capture the distribution of molecular markers such as antibody staining and gene expression *in situ* using common molecular biological and histological techniques. Of course, on living specimens that are small and transparent, OPT can be performed without processing, and at the time of writing, live OPT imaging experiments are being performed.

A subset of the volumetric imaging tools are designed to image living specimens: OCT, SPIM, and MRM. OCT, a reflected light modality, requires no extrinsic labels and is ideal for optical imaging deep within specimens, and for following motions such as blood flow. SPIM offers an important tool at the confluence of imaging and molecular biology technologies, as it is a fluorescent optical sectioning technique, ideal for capturing the expression of GFP reporter genes in living specimens. The use of transgenic GFP reporter constructs allows for the direct *in vivo* visualization of gene transcription during development within the context of the living embryo: the SPIM sample chamber is designed for maintaining physiological conditions and the use of the light sheet minimizes sample bleaching and reduces blur from structures not in the focus plane. Using SPIM, dynamic events ranging from fractions of a second to days can be recorded at voxel sizes of ~0.5 µm.

MRM is not an optical modality and therefore is not limited by the optical properties of the subject. MRM is non-invasive and allows long-term observation of living biological specimens as no ionizing radiation is employed. Although MRM is slower, more expensive, and offers lower resolution than most optical methods, it offers direct observation of morphogenic movements in opaque embryos. Previously, these movements could only be inferred from static sections. Clinically, MRI has a proven diagnostic history but is only in its infancy as a microscopic technique. Tools proven in the clinic are being modified for microscopic use, promising a growing set of techniques for following tissue fine structure and blood flow.

As with any review of finite length, there are a great many modalities and modifications to existing techniques that have not been treated here. Adapting non-conventional elements to conventional devices pushes microscopy development forward. The field of view of confocal microscopy has been greatly increased ($20\,\mathrm{mm}^2$ at 2 µm resolution) with the use of a high-NA f-theta telecentric objective (Dixon, 1995). Microscopic versions of clinical imaging tools are emerging and improving at an alarming rate. These include positron emission tomography (micro-PET), and ultrasonography (micro-US). Typing in any of these key terms in a Web- or library-based search will find a rapidly growing set of offerings. The resolution of these techniques has improved dramatically. The omission of these powerful approaches is in no way intended to diminish their potential role for volumetric imaging, but instead a statement of how rapidly these fields are advancing. The future will see the toolkit for volumetric imaging grow at an increasing rate.

ACKNOWLEDGMENTS

The authors thank Jeff Fingler for additional expert OCT content.

REFERENCES

Allen, M.J., and Meade, T.J., 2004, Magnetic resonance contrast agents for medical and molecular imaging. *Met. Ions. Biol. Syst.* 42:1–38.

Aoki, I., Wu, Y.J., Silva, A.C., Lynch, R.M., and Koretsky, A.P., 2004, *In vivo* detection of neuroarchitecture in the rodent brain using manganese-enhanced MRI, *Neuroimage* 22:1046–1059.

As, H.V., and Lens, P., 2001, Use of 1H NMR to study transport processes in porous biosystems, *J. Ind. Microbiol. Biotechnol*. 26:43–52.

Bock, N.A., Konyer, N.B., and Henkelman, R.M., 2003, Multiple-mouse MRI, *Magn. Reson. Med*. 49:158–167.

Boppart, S.A., Bouma, B.E., Pitris, C., Southern, J.F., Brezinski, M.E., and Fujimoto, J.G., 1998, *In vivo* cellular optical coherence tomography imaging, *Nat. Med*. 4:861–865.

Boppart, S.A., Brezinski, M.E., Bouma, B.E., Tearney, G.J., and Fujimoto, J.G., 1996, Investigation of developing embryonic morphology using optical coherence tomography, *Dev. Biol*. 177:54–63.

Boppart, S.A., Tearney, G.J., Bouma, B.E., Southern, J.F., Brezinski, M.E., and Fujimoto, J.G., 1997, Noninvasive assessment of the developing *Xenopus* cardiovascular system using optical coherence tomography, *Proc. Natl. Acad. Sci. USA* 94:4256–4261.

Callaghan, P.T., 1991, *Principles of Nuclear Magnetic Resonance Microscopy*, Oxford University Press, Oxford, United Kingdom.

Chapon, C., Franconi, F., Roux, J., Marescaux, L., Le Jeune, J.J., and Lemaire, L., 2002, In utero time-course assessment of mouse embryo development using high resolution magnetic resonance imaging, *Anat. Embryol.* 206(1–2):131–137.

Ciobanu, L., and Pennington, C.H., 2004, 3D micron-scale MRI of single biological cells, *Solid State Nucl. Magn. Reson*. 25:138–141.

Dhenain, M., Ruffins, S.W., and Jacobs, R.E., 2001, Three-dimensional digital mouse atlas using high-resolution MRI, *Dev. Biol*. 232:458–470.

Dixon, A.E., Damaskinos, S., Ribes, A., and Beesley, K.M., 1995, A new confocal scanning beam laser macroscope using a telecentric, f-theta laser scan lens, *J. Microsc*. 178:261–266.

Edzes, H.T., van Dusschoten, D., and Van As, H., 1998, Quantitative T2 imaging of plant tissues by means of multi-echo MRI microscopy, *Magn. Reson. Imaging* 16(2):185–96.

Ewald, A.J., McBride, H., Reddington, M., Fraser, S.E., and Kerschmann, R., 2002, Surface imaging microscopy, an automated method for visualizing whole embryo samples in three dimensions at high resolution, *Dev. Dyn*. 225:369–375.

Ewald, A.J., Peyrot, S.M., Tyszka, J.M., Fraser, S.E., and Wallingford, J.B., 2004, Regional requirements for Dishevelled signaling during *Xenopus* gastrulation: Separable effects on blastopore closure, mesendoderm internalization and archenteron formation, *Development* 131:6195–6209.

Fercher, A.F., 1996, Optical coherence tomography, *J. Biomed. Opt*. 1:157–173.

Foster-Gareau, P., Heyn, C., Alejski, A., and Rutt, B.K., 2003, Imaging single mammalian cells with a 1.5 T clinical MRI scanner, *Magn. Reson. Med*. 49:968–971.

Grant, S.C., Buckley, D.L., Gibbs, S., Webb, A.G., and Blackband, S.J., 2001, MR microscopy of multicomponent diffusion in single neurons, *Magn. Reson. Med*. 46:1107–1112.

Haskell, R.C., Williams, M.E., Petersen, D.C., *et al*., 2004, Visualizing early frog development with motion-sensitive 3-D optical coherence microscopy, In: *Proceedings of the 26th Annual International Conference of the IEEE EMBS*, IEEE, San Francisco, CA, USA.

Herman, G.T., 1980, *Image Reconstruction from Projections: The Fundamentals of Computerized Tomography*, Academic Press, San Francisco.

Hinds, K.A., Hill, J.M., Shapiro, E.M., *et al*., 2003, Highly efficient endosomal labeling of progenitor and stem cells with large magnetic particles allows magnetic resonance imaging of single cells, *Blood* 102:867–872.

Hoeling, B.M., Fernandez, A.D., Haskell, R.C., and Petersen, D.C., 2001, Phase modulation at 125 kHz in a Michelson interferometer using an inexpensive piezoelectric stack driven at resonance, *Rev. Sci. Instrum.* 72:1630–1633.

Hoeling, B.M., Fernandez, A.D., Haskell, R.C., Huang, E., Meyers, W.R., Petersen, D.C., Ungersma, S.E., Wang, R., and Williams, M.E., 2000, An optical coherence microscope for 3-dimensional imaging in developmental biology, *Opt. Express* 6:136–146.

Holdsworth, D.W., and Thornton, M.M., 2002, MicroCT in small animal and specimen imaging, *Trends Biotechnol*. 20(Suppl.):S34–S39.

Huang, D., Swanson, E.A., Lin, C.P., Schuman, J.S., Stinson, W.G., Chang, W., Hee, M.R., Flotte, T., Gregory, K., Puliafito, C.A., Fujimoto, J.G., 1991, Opt. Coherence Tomogr. *Sci.* 254:1178–1181.

Huisken, J., Swoger, J., Del Bene, F., Wittbrodt, J., and Stelzer, E.H.K., 2004, Optical sectioning deep inside live embryos by selective plane illumination microscopy, *Science* 305:1007–1009.

Izatt, J.A., Kulkarni, M.D., Wang, H.-W., Kobayashi, K., and Sivak, M.V. Jr., 1996, Optical coherence tomography and microscopy in gastrointestinal tissues, *IEEE J. Sel. Topics Quant. Electron.* 2:1017–1028.

Jacobs, R.E., Ahrens, E.T., Dickinson, M.E., and Laidlaw, D., 1999, Towards a microMRI atlas of mouse development, *Comput. Med. Imaging Graph.* 23(1):15–24.

Jacobs, R.E., Papan, C., Ruffins, S., Tyszka, J.M., and Fraser, S.E., 2003, MRI: Volumetric imaging for vital imaging and atlas construction, *Nat. Cell Biol*. Ss10–Ss16.

Jiang, Y., Pandya, K., Smithies, O., and Hsu, E.W., 2004, Three-dimensional diffusion tensor microscopy of fixed mouse hearts, *Magn. Reson. Med*. 52:453–460.

Johnson, G.A., Benveniste, H., Black, R.D., Hedlund, L.W., Maronpot, R.R., and Smith, B.R., 1993, Histology by magnetic resonance microscopy, *Magn. Reson. Q* 9:1–30.

Johnson, G.A., Cofer, G.P., Fubara, B., Gewalt, S.L., Hedlund, L.W., and Maronpot, R.R., 2002a, Magnetic resonance histology for morphologic phenotyping, *J. Magn. Reson. Imaging* 16:423–429.

Johnson, G.A., Cofer, G.P., Gewalt, S.L., and Hedlund, L.W., 2002b, Morphologic phenotyping with MR microscopy: The visible mouse, *Radiology* 222:789–793.

Keng, W.T., Sharpe, J., *et al*., 2002, Optical projection tomographic examination of miscarried human embryos, *J. Med. Genet*. 39:S23–S23.

Kerwin, J., Scott, M., Sharpe, J., *et al*., 2004, 3 dimensional modelling of early human brain development using optical projection tomography, *BMC Neurosci*. 5:27–27.

Kockenberger, W., 2001, Nuclear magnetic resonance micro-imaging in the investigation of plant cell metabolism, *J. Exp. Bot*. 52(356):641–652.

Kockenberger, W., De Panfilis, C., Santoro, D., Dahiya, P., and Rawsthorne, S., 2004, High resolution NMR microscopy of plants and fungi, *J. Micros.* 214(Pt2):182–189.

Kovacevic, N., Henderson, J.T., Chan, E., *et al.*, 2005, A three-dimensional MRI atlas of the mouse brain with estimates of the average and variability, *Cereb. Cortex.* 15(5):639–645.

Kuchenbrod, E., Kahler, E., Thurmer, F., Deichmann, R., Zimmermann, U., and Haase, A., 1998, Functional magnetic resonance imaging in intact plants–quantitative observation of flow in plant vessels, *Magn. Reson. Imaging* 16:331–338.

Lee, S.C., Kim, K., and Kim, J., 2001, One micrometer resolution NMR microscopy, *J. Magn. Reson*. 150:207–213.

Lo, C., Nabel, E., and Balahan, R., 2003, Meeting report: NHLBI symposium on phenotyping: Mouse cardiovascular function and development, *Physiol. Genomics* 13(3):185–186.

Louie, A.Y., Huber, M.M., Ahrens, E.T., *et al.*, 2000, In vivo visualization of gene expression using magnetic resonance imaging. *Nat. Biotechnol.* 18(3):321–325.

Mansfield, P., 1977, Multi-planar image formation using NMR spin echoes, *J. Phys. C* 10:L55–L58.

Manz, B., Volke, F., Goll, D., and Horn, H., 2003, Measuring local flow velocities and biofilm structure in biofilm systems with magnetic resonance imaging (MRI), *Biotechnol. Bioeng*. 84:424–432.

Masters, B.R., 1999, Early development of optical low-coherence reflectometry and some recent biomedical applications, *J. Biomed. Opt*. 4:236–247.

Matsuda, Y., Utsuzawa, S., Kurimoto, T., 2003, Super-parallel MR microscope, *Magn. Reson. Med*. 50:183–189.

Papan, C., Velan, S.S., Fraser, S.E., and Jacobs, R.E., 2001, 3D time-lapse analysis of *Xenopus* gastrulation movements using mu MRI, *Dev. Biol*. 235:189.

Paterson-Beedle, M., Nott, K.P., Macaskie, L.E., and Hall, L.D., 2001, Study of biofilm within a packed-bed reactor by three-dimensional magnetic resonance imaging, *Methods Enzymol*. 337:285–305.

Paulus M.J., Gleason, S.S., Easterly, M.E., and Foltz, C.J., 2001, A review of high resolution X-ray computed tomography and other imaging modalities for small animal research, *Lab. Animal* 30(3):36–45.

Paulus, M.J., Gleason, S.S., Kennel, S.J., Hunsicker, P.R., and Johnson, D.K., 2000, High-resolution x-ray computed tomography: An emerging tool for small animal cancer research, *Neoplasia* 2:62–70.

Pautler, R.G., and Koretsky, A.P., 2002, Tracing odor-induced activation in the olfactory bulbs of mice using manganese-enhanced magnetic resonance imaging, *Neuroimage* 16:441–448.

Pautler, R.G., Mongeau, R., and Jacobs, R.E., 2003, *In vivo* trans-synaptic tract tracing from the murine striatum and amygdala utilizing manganese enhanced MRI (MEMRI), *Magn. Reson. Med*. 50:33–39.

Pickhardt, P.J., Halberg, R.B., Taylor, A.J., Durkee, B.Y., Fine, J., Lee, Jr., F.T., and Weichert, J.P., 2005, Microcomputed tomography colonography for polyp detection in an *in vivo* mouse tumor model. *PNAS* 102:3419–3422.

Pierpaoli, C., Jezzard, P., Basser, P.J., Barnett, A., and DiChiro, G., 1996, Diffusion tensor MR imaging of the human brain, *Radiology* 201:637–648.

Robson, S.C., Woods, H.M., *et al*., 2004, 3-dimensional modelling of human development using optical projection tomography, *J. Soc. Gynecol*. *Invest*. 11:296A.

Rollins, A.M., and Izatt, J.A., 1999, Optimal interferometer designs for optical coherence tomography, *Opt. Lett*. 24:1484–1486.

Rollins, A.M., Kulkarni, M.D., Yazdanfar, S., Ung-arunyawee, R., and Izatt, J.A., 1998, *In vivo* video rate optical coherence tomography, *Opt. Express* 3:219–229.

Segars, W.P., Tsui, B.M., Frey, E.C., Johnson, G.A., and Berr, S.S., 2004, Development of a 4-D digital mouse phantom for molecular imaging research, *Mol. Imaging Biol*. 6:149–159.

Seymour, J.D., Codd, S.L., Gjersing, E.L., and Stewart, P.S., 2004, Magnetic resonance microscopy of biofilm structure and impact on transport in a capillary bioreactor, *J. Magn. Reson*. 167:322–327.

Shapiro, E.M., Skrtic, S., Sharer, K., Hill, J.M., Dunbar, C.E., and Koretsky, A.P., 2004, MRI detection of single particles for cellular imaging, *Proc. Natl. Acad. Sci. USA* 101:10901–10906.

Sharpe, J., 2003, Optical projection tomography as a new tool for studying embryo anatomy, *J. Anat.* 202:175–181.

Sharpe, J., 2004, Optical projection tomography, *Annu. Rev. Biomed. Eng*. 6:209–228.

Sharpe, J., Ahlgren, U., Perry, P., *et al.*, 2002, Optical projection tomography as a tool for 3D microscopy and gene expression studies, *Science* 296:541–545.

Song, S.K., Sun, S.W., Ramsbottom, M.J., Chang, C. Russell, J., and Cross, A.H., 2002, Dysmyelination revealed through MRI as increased radial (but unchanged axial) diffusion of water, *Neuroimage* 17:1429–1436.

Tearney, G.J., Bouma, B.E., Boppart, S.A., Golubovic, B., Swanson, E.A., and Fujimoto, J.G., 1996, Rapid acquisition of *in vivo* biological images by use of optical coherence tomography, *Opt. Lett.* 21:1408–1410.

Tearney, G.J., Brezinski, M.E., Bouma, B.E., Boppart, S.A., Pitris, C., Southern, J.F., and Fujimoto, J.G., 1997, *In vivo* endoscopic optical biopsy with optical coherence tomography, *Science* 276:2037–2039.

Tuch, D.S., Reese, T.G., Wiegell, M.R., and Wedeen, V.J., 2003, Diffusion MRI of complex neural architecture, *Neuron* 40:885–895.

Weichert, J.P., 2004, Micro-computed tomography of mouse cancer models, *In: Mouse Models of Human Cancer* (E.C. Holland, ed.), John Wiley and Sons, New York, pp. 339–348.

Weinmann, H.J., Brasch, R.C., Press, W.R., and Wesbey, G.E., 1984, Characteristics of gadolinium-DTPA complex: A potential NMR contrast agent, *AJR Am J Roentgenol* 142:619–624.

Weinmann, H.J., Ebert, W., Misselwitz, B., and Schmitt-Willich H., 2003, Tissue-specific MR contrast agents, *Eur. J. Radiol*. 46:33–44.

Weninger, W., and Mohun, T., 2002, Cardiac phenotyping of transgenic embryos: A rapid 3D-screening method based on episcopic fluorescence imaging capturing (EFIC), *Clin. Exp. Pharmacol. Physiol.* 29:A70–A71.

Wojtkowski, M., Srinivasan, V.J., Ko, T.H., Fujimoto, J.G., Kowalczyk, A., and Duker, J.S., 2004, Ultrahigh-resolution, high-speed, Fourier domain optical coherence tomography and methods for dispersion compensation, *Optics. Express* 12(11):2404–2422.

Yazdanfar, S., Kulkarni, M.D., and Izatt, J.A., High resolution imaging of *in vivo* cardiac dynamics using color Doppler optical coherence tomography, *Opt. Express* 1:424–431.

Zhang, J., Richards, L.J., Yarowsky, P., Huang, H., van Zijl, P.C., and Mori, S., 2003, Three-dimensional anatomical characterization of the developing mouse brain by diffusion tensor microimaging, *Neuroimage* 20: 1639–1648.